Analysis of hyperspherical adiabatic curves of helium: A classical dynamics study

N. S. Simonović
Institute of Physics, University of Belgrade, P. O. Box 57, 11001 Belgrade, Serbia

E. A. Solov'ev
Bogoliubov Laboratory of Theoretical Physics, Joint Institute for Nuclear Research, 141980 Dubna, Russia
(Received 25 February 2013; published 6 May 2013)

The hyperspherical adiabatic curves (adiabatic eigenenergies as functions of the hyperradius R) of helium for zero total angular momentum are analyzed by studying the underlying classical dynamics which in the adiabatic treatment reduces to constrained two-electron motion on a hypersphere. This dynamics supports five characteristic classical configurations which can be represented by five types of short periodic orbits: the frozen planet (FP), the inverted frozen planet (IFP), the asymmetric stretch (AS), the asynchronous (ASC), and the Langmuir periodic orbit (PO). These POs are considered as fundamental modes of the two-electron motion on a hypersphere which, after quantization, give five families of so-called adiabatic lines (adiabatic energies related to these POs as functions of R). It is found that multiplets, each of them consisting of adiabatic curves which converge to the same ionization threshold, are at large values of R delimited from the bottom and from the top by the adiabatic lines which are related to the IFP and stable AS POs and to the FP PO, respectively. At smaller values of R, where the AS PO becomes unstable, the curves move to the area between the ASC (bottom) and AS (top) lines by crossing the latter. Therefore, at different values of R the lower limiting line of the multiplet is related to the three types of PO (IFP, AS, and ASC), which are all stable in the negative-energy part of this line. As a consequence, the quantum states of helium in principle are not related individually to a single classical configuration on the hypersphere. In addition, it is demonstrated that "unstable parts" of adiabatic lines (the so-called diabatic curves) determine the positions and type of avoided and hidden crossings between hyperspherical adiabatic curves. Two clearly visible classes of avoided crossings are related to the AS and ASC POs. In addition, a number of avoided crossings of the adiabatic curves is observed at the positions where the adiabatic lines that are related to different types of PO cross mutually. Finally, a class of hidden crossings which is located near the saddle point of the potential is related to the Langmuir orbit. The large spacing between adiabatic curves at the positions of these hidden crossings is explained by high instability of the Langmuir PO compared to the AS and ASC POs.

DOI: 10.1103/PhysRevA.87.052503 PACS number(s): 31.15.xg, 31.15.xj, 31.50.Gh

I. INTRODUCTION

In atomic and molecular physics the adiabatic approach has been used to study a number of different problems including (i) those related to bound and resonant states as well as (ii) scattering and fragmentation processes (collisions). The adiabatic treatment involves approximate separation of the "fast" and "slow" components of motion of the atomic or molecular system in such a way that the energy eigenvalues of the fast subsystem emerge as effective potentials governing the motion of the slow one. For molecular systems this approach arises naturally due to the large difference between the frequencies of electronic and nuclear motions. Here the internuclear distances appear as the adiabatic (slow) variables whereas the effective (adiabatic) potential is determined by the electronic motion (the Born-Oppenheimer approximation). Then, as is well known, the vibrational and rotational states and energy levels of a molecular system can be obtained by solving the eigenvalue problem for nuclear motion in this effective potential.

Due to the different time scales of electronic and nuclear motions the adiabatic approach (based on the Born-Fock adiabatic theorem [1]) is also one of the most powerful methods in the theory of slow atomic collisions. The main point in this theory is that the inelastic transitions between electronic adiabatic states occur at the place of the closest approach of adiabatic potential curves—avoided crossings (anticrossings). According to the von Neumann–Wigner theorem [2], the exact crossing of two adiabatic potential curves of the same symmetry is forbidden; however, every avoided crossing of such curves reflects their exact crossing at a complex branch point joining two sheets of the Riemann surface of the (complex) adiabatic potential. Then the probability of inelastic transition can be expressed through a contour integral of the energy difference between two sheets corresponding to the initial and final adiabatic states around the branch point (see [3] and references therein). Initially, in the application of the adiabatic approach the narrow avoided crossings of adiabatic potential curves with the Landau-Zener type of couplings [4,5] were used. These avoided crossings are related to the under-barrier resonant interactions between electronic states located in different regions of configuration space, e.g., on different nuclei in ion-atom collisions. Later, a different mechanism of nonadiabatic transitions via the so-called "hidden crossings" was discovered [6]. It is shown that such transitions are dominant in atomic collisions and provide a complete description of inelastic processes. In the case of hidden crossings the branch points lie deeper in the complex plane and thus the adiabatic curves at the positions of anticrossings are more separated than in the case of the Landau-Zener couplings. For this reason, often they are not manifested in the pattern of the potential curves at real values

of the adiabatic parameter. Hidden crossings happen when an electronic energy level touches the top of an effective potential barrier. On the other hand, in the classical description, the full-dimensional electronic trajectory at this place collapses into an unstable periodic orbit (PO). On the basis of this correspondence a semiclassical theory of hidden crossings was developed [7]. Within this description the unstable periodic orbits generate the hidden crossings of adiabatic energy levels. The position of a hidden crossing occurs at the place where a quantized trajectory approaches the corresponding unstable PO, whereas the probability of inelastic transition via this hidden crossing is determined by the Lyapunov exponent λ of this PO. In detail, the theory is discussed in the review paper presented in Ref. [8].

The adiabatic approach (of the Born-Fock type) is applicable also to an arbitrary Coulomb few-body system if it is possible to find a set of coordinates which makes the dynamics approximately separable. Hence, the so-called hyperspherical adiabatic approach [9] is one of the most successful methods for describing the singly and doubly excited states of two-electron atoms. The success of this approach lies in the capability of hyperspherical coordinates to describe adequately the collective modes of two-electron dynamics. The electrons radial coordinates r_1 and r_2 are here replaced by the hyperradius $R = (r_1^2 + r_2^2)^{1/2}$ and the hyperangle $\alpha = \arctan(r_2/r_1)$ $(0 \leqslant \alpha \leqslant \pi/2)$ which measure the size of the system and the radial correlation of the electrons, respectively. The angular correlation can be described by the mutual angle $\vartheta = \angle(\mathbf{r}_1,\mathbf{r}_2)$. The other three (Euler) angles specify the orientation of the atom. The hyperspherical approach is based on the adiabatic expansion of the two-electron wave function where the adiabatic ("channel") functions are obtained by solving the Schrödinger equation at fixed values of the hyperradius R—the so-called hyperspherical adiabatic eigenvalue problem. For a given symmetry $(^{2S+1}L^{\pi})$ and a given ionization threshold (determined by the quantum number N of the "inner" electron) the channel index μ can be expressed by the set of approximate quantum numbers $(K,T)^A$ [10,11]. Each channel is related to a hyperspherical adiabatic energy (potential) curve which connects the eigenvalues of a given channel index at different values of R. Although it is not obvious that the adiabatic approximation should be valid in atomic systems, the approximation has considerable validity, apparently because of the slow variation of the Coulomb interaction as the system expands.

Except for the helium atom the hyperspherical approach has been successfully applied in treatments of bound states and resonances of heliumlike ions and other Coulomb three-body systems (see Ref. [12] for a review). Also, it should be mentioned that the adiabatic treatment of Coulomb three-body systems is not feasible in hyperspherical coordinates exclusively. The so-called molecular approximation, where the interelectronic distance is treated as an adiabatic variable, is an even more direct generalization of the Born-Oppenheimer approximation to two-electron systems (see, e.g., Refs. [13,14]). Both adiabatic approximations, however, reveal similar key features of the two-electron and Coulomb three-body systems generally.

Analogously to the hidden-crossing theory of slow atomic collisions, the nonadiabatic transitions between hyperspherical adiabatic states can be used for describing atomic collisions with light particles. This method has been applied in studies of ionization of hydrogen by electron impact [15,16] and positronium formation in positron-hydrogen collisions [17]. A classification of hidden crossings in the three-body Coulomb problem has been studied within the hyperspherical adiabatic approach as well as using the approximate separability of the hyperspherical adiabatic eigenvalue problem in hyperspherical elliptic coordinates. The results are illustrated by calculations for the positronium negative ion $(e^-e^+e^-)$ for zero total angular momentum where two classes of hidden crossings are recognized and related to two types of short POs [18].

The main idea of this paper is to explain some basic properties of the hyperspherical adiabatic curves (multiplet structure, asymptotic behavior, avoided and hidden crossings, etc.) of two-electron atomic systems, particularly for the helium atom, using classical dynamics as a tool. Since the hyperspherical adiabatic curves are determined by treating the hyperradius R as a parameter, the underlying classical dynamics is not defined in the full phase space, but for each value of R we have to consider the constrained two-electron motion lying on the hypersphere of this hyperradius $(\mathbf{r}_1^2 + \mathbf{r}_2^2 = R^2)$. In this paper we restrict our analysis to the case when the total angular momentum is zero. Then all three Euler angles are fixed, the (full) system has three degrees of freedom (which can be related to the R, α, and ϑ coordinates), and the configuration space of the constrained motion (for a given R) is the two-dimensional (2D) surface of the corresponding hypersphere. In the next section we study classical configurations on a hypersphere for the helium atom (for different values of the parameter R) and analyze properties of the shortest POs. In Sec. III we perform the quantization of these POs and obtain the corresponding adiabatic energies which are in Sec. IV used in the analysis of the hyperspherical adiabatic curves. A summary and conclusions are presented in Sec. V. A brief preliminary analysis is given in a recent review paper [19].

II. CLASSICAL DYNAMICS ON A HYPERSPHERE

A. The Hamiltonian function, scaling properties, and symmetries

The Hamiltonian function of two-electron atoms in hyperspherical coordinates R, α, and ϑ, for the total angular momentum $L = 0$, reads (in the approximation of an infinitely heavy nucleus)

$$H(P_R,P_\alpha,P_\vartheta,R,\alpha,\theta) = \frac{1}{2}\left(P_R^2 + \frac{P_\alpha^2}{R^2} + \frac{P_\vartheta^2}{R^2\sin^2\alpha\cos^2\alpha}\right) + \frac{C(\alpha,\vartheta)}{R}, \quad (1)$$

$$C(\alpha,\vartheta) = -\frac{Z}{\sin\alpha} - \frac{Z}{\cos\alpha} + \frac{1}{\sqrt{1-\sin 2\alpha\cos\vartheta}}, \quad (2)$$

where P_R, P_α, and P_ϑ are the canonically conjugated momenta and Z is the nuclear charge.

If the hyperradius is fixed ($R = \text{const}$), then $P_R = 0$ and the Hamiltonian function (1) reduces to

$$H_R(P_\alpha,P_\vartheta,\alpha,\theta) = \frac{1}{2R^2}\left(P_\alpha^2 + \frac{P_\vartheta^2}{\sin^2\alpha\cos^2\alpha}\right) + \frac{C(\alpha,\vartheta)}{R}. \quad (3)$$

The motion determined by this Hamiltonian function is constrained to lie on the hypersphere of hyperradius R. Formally, this system belongs to the class of holonomic mechanical systems, because it obeys the constraint $\mathbf{r}_1^2 + \mathbf{r}_2^2 - R^2 = 0$. Using atomic physics vocabulary, the motion determined by the Hamiltonian function (3) is always bound, in contrast to the real dynamics determined by the Hamiltonian function (1). However, although the number of degrees of freedom for the constrained system is reduced to 2, due to the coupling between the α and ϑ variables by the potential $C(\alpha,\vartheta)/R$, this system is still nonintegrable and the corresponding classical dynamics is mixed (both regular and chaotic).

Due to the scaling properties of Coulomb systems, it is sufficient to calculate the trajectories and all classical quantities for one fixed value of the hyperradius. If ϵ, τ, and s are the values for the energy, time, and action, respectively, at $R = 1$, the corresponding values for an arbitrary R are

$$E = \epsilon/R, \quad t = R^{3/2}\tau, \quad S = \sqrt{R}\,s. \tag{4}$$

Then, the scaled potential is $C(\alpha,\vartheta)$ and the scaled Hamiltonian function $h = RH_R$ has the form

$$h(p_\alpha,p_\vartheta,\alpha,\theta) = \frac{1}{2}\left(p_\alpha^2 + \frac{p_\vartheta^2}{\sin^2\alpha\cos^2\alpha}\right) + C(\alpha,\vartheta), \tag{5}$$

where $p_\alpha = P_\alpha/\sqrt{R}$ and $p_\vartheta = P_\vartheta/\sqrt{R}$ are the scaled momenta.

The potential $C(\alpha,\vartheta)$ [and thus $C(\alpha,\vartheta)/R$ for any fixed value of R] is characterized by three symmetry axes: (i) $\alpha = \pi/4$, (ii) $\vartheta = 0$, and (iii) $\vartheta = \pi$. These axes are essentially one-dimensional (1D) invariant subspaces of the 2D configuration space $\{\alpha,\vartheta\}$, because the constrained electronic motion which initially lies in one of them will remain there for all times. [This definition is analogous to that for the symmetry planes in the three-dimensional configuration space for unconstrained motion [20].] The first (i) symmetry axis corresponds to symmetric motion of the electrons where $r_1 = r_2$ (the so-called Wannier ridge). The other two axes correspond to collinear configurations with the electrons moving: (ii) on the same side of the nucleus (the *Zee* configuration) and (iii) on different sides of the nucleus (the *eZe* configuration). The position of the crossing of axes (i) and (iii) ($\alpha = \pi/4$, $\vartheta = \pi$) is the saddle point of the potential $C(\alpha,\vartheta)$, which at this point takes the value $\epsilon_{\rm sp} = C(\pi/4,\pi) = (1-4Z)/\sqrt{2}$. For $Z = 2$ one has $\epsilon_{\rm sp} = -7/\sqrt{2} \approx -4.949\,75$ (see Fig. 1).

The classical trajectories are calculated numerically by integrating the corresponding equations of motion. We emphasize that the original equations [Hamilton's equations associated with the Hamiltonian function (3) or (5)] before integrating must be regularized in order to remove the singularities of the potential (see the Appendix). Although classical dynamics does not account automatically for the Pauli principle (the correspondence between classical trajectories and quantum states of different symmetries is considered in Sec. III), the particle exchange symmetry of the Hamiltonian function reduces the accessible configuration space to the fundamental domain $\alpha \in [0,\pi/4]$, i.e., to the desymmetrized region of configuration space with $r_1 > r_2$. Except for the semiclassical quantization, this reduction is particularly suitable in the regularization procedure (see the Appendix). However, for convenience, the classical trajectories in this section will be given in the full (2D) configuration space for the constrained motion.

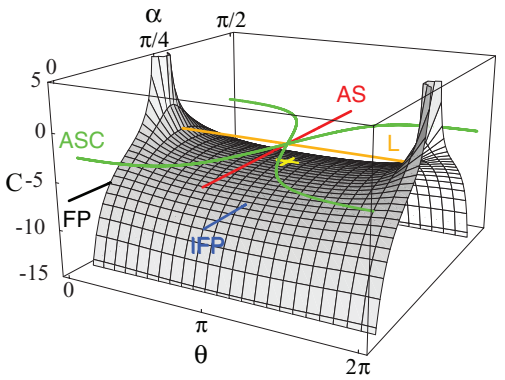

FIG. 1. (Color online) The potential $C(\alpha,\vartheta)$ for the helium atom ($Z = 2$) and examples for short periodic orbits at fixed hyperradius: the frozen planet (FP, black line), inverted frozen planet (IFP, blue line), asymmetric stretch (AS, red line), asynchronous (ASC, green line), and Langmuir (L, orange line) POs. The yellow cross denotes the position of the saddle point.

B. Phase-space structure and short periodic orbits

The phase-space structure is examined using the Poincaré surfaces-of-section technique. For Hamiltonian systems with two degrees of freedom (four-dimensional phase space) the classical motion is confined to the energy shell which is three-dimensional and the Poincaré surface of section is a two-dimensional cut of this shell (see, e.g., [21]). As is well known each periodic orbit generates fixed points in the section. If the orbit is, however, quasiperiodic it generates an invariant curve instead of fixed points. The type of fixed point is determined by the behavior of the invariant curves in its vicinity. Elliptic fixed points (i.e., the fixed points surrounded by elliptic invariant curves) are linearly stable, since an arbitrary point in its vicinity stays there after arbitrary iterations. On the other hand, if the invariant curves are hyperbolic, we have hyperbolic fixed points, which are unstable. Chaotic orbits densely fill a finite volume on the three-dimensional energy shell and appear rather as areas in the Poincaré section. Due to their unstable character, these chaotic regions usually appear around hyperbolic fixed points.

In our case it is convenient to construct the surfaces of section as cuts of the energy shell $h(p_\alpha,p_\vartheta,\alpha,\vartheta) = \epsilon$ along the potential symmetry lines. In Fig. 2 we show the cut (α,p_α) of the ϵ shell at $\vartheta = \pi$, i.e., the surface of section

$$\{(\alpha,p_\alpha)|\ \exists\ p_\vartheta : h(p_\alpha,p_\vartheta,\alpha,\pi) = \epsilon\} \tag{6}$$

for several scaled energies. The condition $h(p_\alpha,p_\vartheta,\alpha,\pi) = \epsilon$ determines the energy-allowed area of section. Using Eq. (5), it takes the explicit form $p_\alpha^2 \leqslant 2[\epsilon - C(\alpha,\pi)]$, where the equality sign corresponds to the case $p_\vartheta = 0$ and this equation defines the boundary lines of the area (shown in the sections in Fig. 2). The sections of this type are particularly convenient

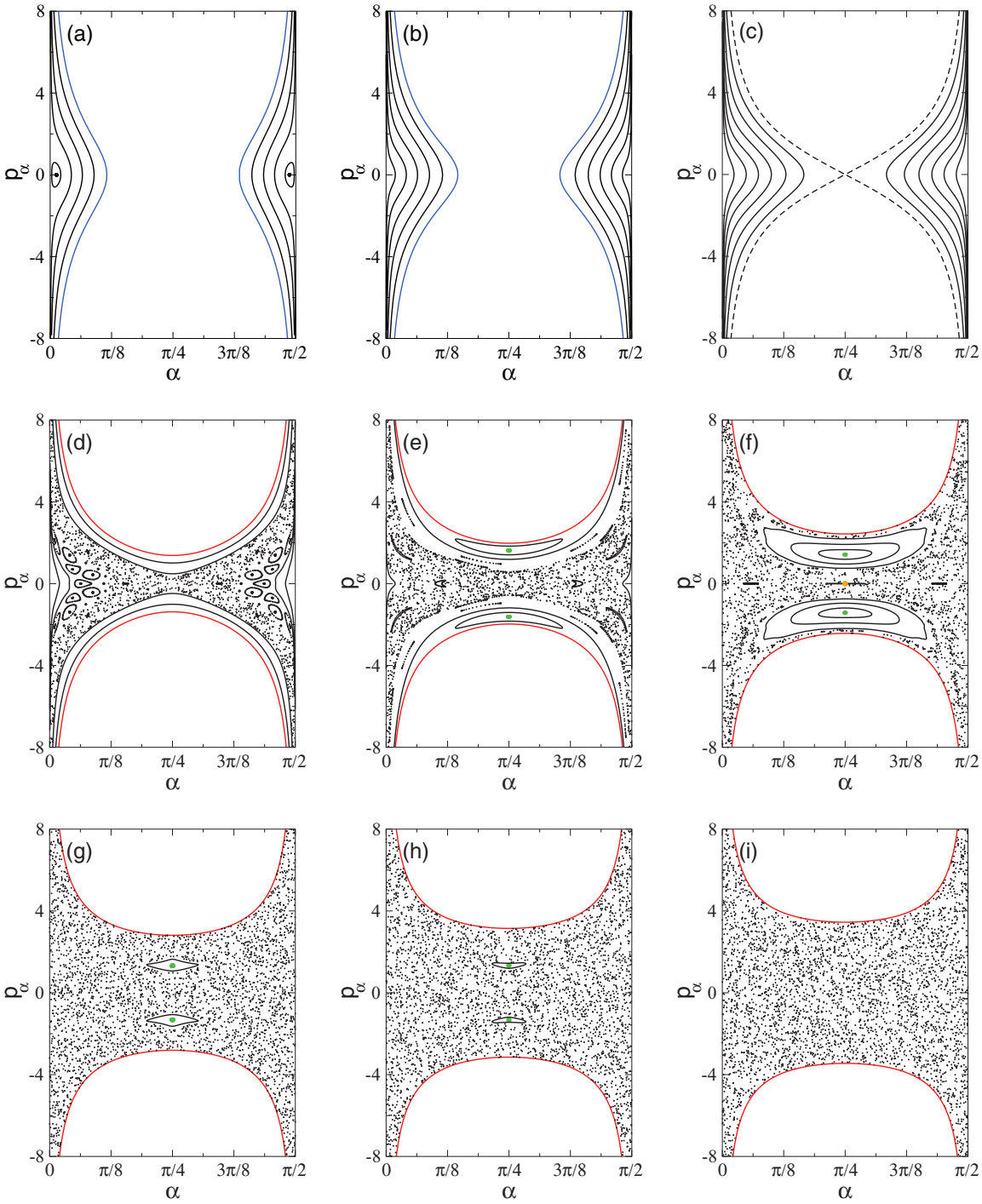

FIG. 2. (Color online) The Poincaré sections (6) (the cuts at $\vartheta = \pi$) for $Z = 2$ at the scaled energies (a) $\epsilon = -7$, (b) $\epsilon = -6$, (c) $\epsilon = \epsilon_{\rm sp} = -4.949\,75$, (d) $\epsilon = -4$, (e) $\epsilon = -3$, (f) $\epsilon = -2$, (g) $\epsilon = -1$, (h) $\epsilon = 0$, and (i) $\epsilon = 1$. The vertical lines $\alpha = 0$ and $\pi/2$ correspond to the FP PO. The boundary lines of the energy-allowed area for $\epsilon < \epsilon_{\rm sp}$ (blue lines) and for $\epsilon > \epsilon_{\rm sp}$ (red lines) correspond to the IFP PO and to the AS PO, respectively. The central fixed point $(\alpha, p_\alpha) = (\pi/4, 0)$ is related to the L PO [stable only in a narrow interval of the scaled energies around $\epsilon = -2$; see the orange dot in the section (f)]. The elliptic fixed points in the sections (e)–(h), located symmetrically below and above the central one, correspond to the ASC PO (green dots).

for localization of off-collinear orbits. On the other hand, the cut (ϑ, p_ϑ) of the ϵ shell at $\alpha = \pi/4$, i.e., the section

$$\{(\vartheta, p_\vartheta) |\ \exists\ p_\alpha : h(p_\alpha, p_\vartheta, \pi/4, \vartheta) = \epsilon\}, \tag{7}$$

shown in Fig. 3 for different ϵ, is more useful to visualize the out-of-phase motion (both collinear and off collinear). The energy-allowed area of this section is determined by the condition $p_\vartheta^2 \leqslant \frac{1}{2}[\epsilon - C(\pi/4, \vartheta)]$. The equality sign corresponds

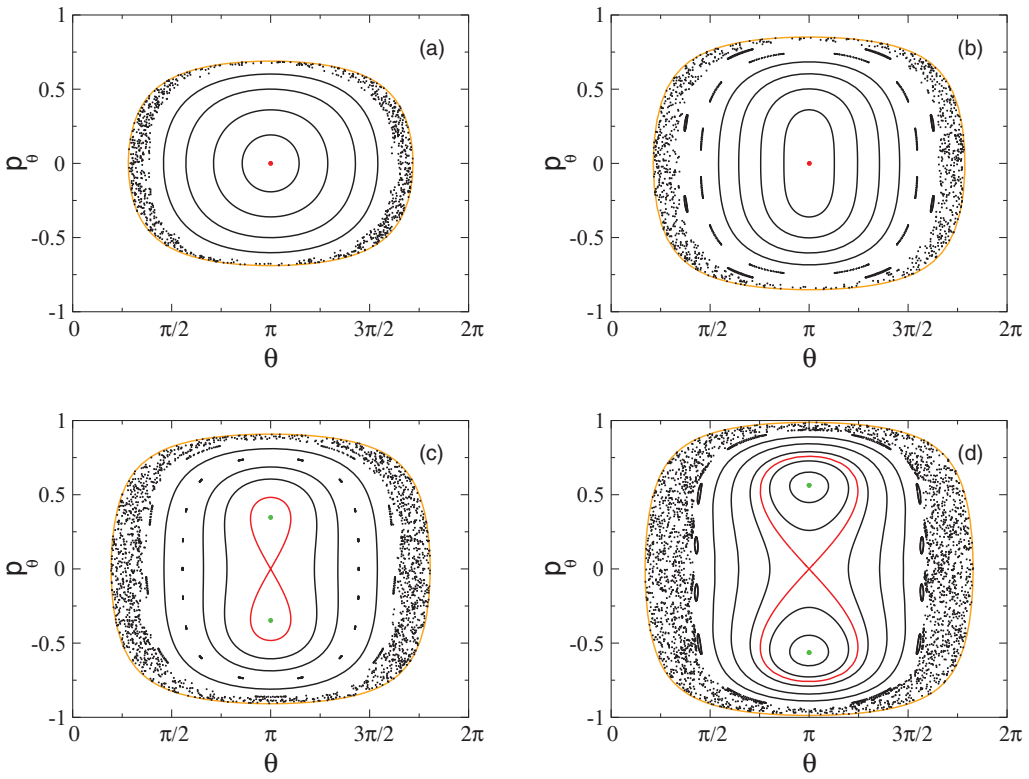

FIG. 3. (Color online) The Poincaré sections (7) (the cuts at $\alpha = \pi/4$) for $Z = 2$ at the scaled energies (a) $\epsilon = -4$, (b) $\epsilon = -3.5$, (c) $\epsilon = -3.3$, and (d) $\epsilon = -3$. The central fixed point (red), which is for $\epsilon < -3.487$ stable [elliptic fixed point; see sections (a) and (b)] and for $\epsilon > -3.487$ unstable [hyperbolic fixed point; see sections (c) and (d)], corresponds to the AS PO. The elliptic fixed points in the sections (c) and (d), located symmetrically below and above the central one (green), correspond to the ASC PO. The boundary line of the energy-allowed area (orange) corresponds to the L PO.

to the case $p_\alpha = 0$, which determines the boundary lines of the energy-allowed area (Fig. 3).

Examinations of the Poincaré sections indicate that five characteristic types of classical configurations exist, which are related to five types of short periodic orbits (POs); see Fig. 1. There are two frozen-planet-type POs—the frozen planet (FP) PO and the inverted frozen planet (IFP) PO, two out-of-phase POs—the asymmetric stretch (AS) PO and the asynchronous (ASC) PO, and an oscillatory Langmuir-type (L) PO. Two of them are off collinear (ASC and L) and the others are collinear ($\vartheta = 0,\pi$ and $P_\vartheta = 0$). Note that these POs, except the IFP PO, have counterparts (of the same names) in the full (unconstrained) two-electron dynamics (see, e.g., [22–25] and also overviews in Refs. [14,20,26]). Some properties of these POs are given in Table I.

TABLE I. Properties of the fundamental (short) periodic orbits of the constrained two-electron system ($R = \text{const}$) with $Z = 2$ (helium). Here $\epsilon_{sp} = -4.950$ and $\epsilon_{bif} = -3.487$.

Periodic orbit (PO)	ϵ domain	Interval of stability
Frozen planet (FP)	$\forall\,\epsilon$	$-6.283 < \epsilon < -2.972$
Inverted frozen planet (IFP)	$\epsilon < \epsilon_{sp}$	Always stable
Asymmetric stretch (AS)	$\epsilon > \epsilon_{sp}$	$\epsilon_{sp} < \epsilon < \epsilon_{bif}$
Asynchronous (ASC)	$\epsilon > \epsilon_{bif}$	$\epsilon_{bif} < \epsilon < 0.261$
Langmuir (L)	$\epsilon > \epsilon_{sp}$	$-2.072 < \epsilon < -1.969$

In the sections of type (6) shown in Fig. 2 the frozen planet PO, which exists for all scaled energies, is represented by the vertical lines $\alpha = 0$ and $\pi/2$. The inverted frozen planet and the asymmetric stretch POs, which, however, exist for $\epsilon < \epsilon_{sp}$ and $\epsilon > \epsilon_{sp}$, respectively (they transform from one to the other at the saddle point), are related to the boundary lines of energy-allowed areas in the corresponding sections. The Langmuir PO (existing also for $\epsilon > \epsilon_{sp}$) is located at the centers of sections $(\alpha, p_\alpha) = (\pi/4,0)$, and, finally, the asynchronous PO, which occurs as a new PO after a bifurcation of the AS PO ($\epsilon > -3.487$ for $Z = 2$), is represented by two elliptic fixed points located symmetrically below and above the central fixed point (L PO).

The Poincaré sections (7), on the other hand, can be constructed only if $\epsilon > \epsilon_{sp}$ (see Fig. 3). In these sections, therefore, there is no fixed point related to the IFP PO, but also since none of them intersects the $\alpha = \pi/4$ surface, there is also no fixed point related to the FP PO. The AS PO is here represented by the central fixed point $(\vartheta, p_\vartheta) = (\pi,0)$, which is stable (an elliptic fixed point) for lower scaled energies. The bifurcation, which for $Z = 2$ occurs around $\epsilon = -3.487$, changes the character of the central fixed point, which becomes hyperbolic (unstable) and two new elliptic fixed points arise. The new fixed points are located symmetrically below and above the central (AS PO) fixed point and correspond to the ASC PO. Finally, the L PO is in these sections represented by the boundary line of the energy-allowed area.

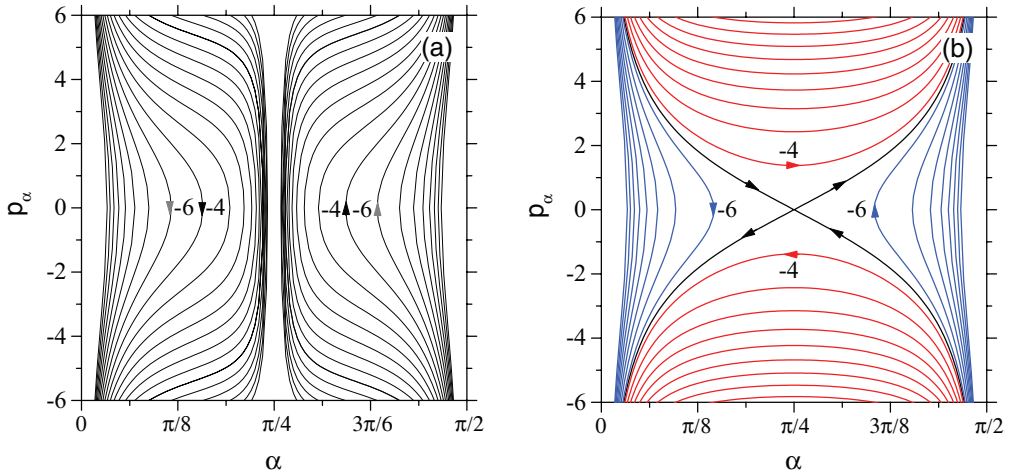

FIG. 4. (Color online) The phase trajectories for $Z = 2$ and different scaled energies ($\epsilon = -20, -18, \ldots, 20$) belonging to (a) the *Zee* collinear configuration and (b) the *eZe* collinear configuration. The infinite potential barrier at $\alpha = \pi/4$ separates the collinear *Zee* motion (the FP orbits) confined in the region $0 < \alpha < \pi/4$ from that in the region $\pi/4 < \alpha < \pi/2$. The *eZe* orbit with $\epsilon = \epsilon_{sp}$ (black lines) is the separatrix dividing the IFP orbits ($\epsilon < \epsilon_{sp}$, blue lines) from the AS orbits ($\epsilon > \epsilon_{sp}$, red lines). The phase trajectories with arrows showing the phase flow are those corresponding to the scaled energies $\epsilon = -6$ (gray, blue), $\epsilon = \epsilon_{sp}$ (separatrix), and $\epsilon = -4$ (black, red).

One can see that at low scaled energies ($\epsilon < \epsilon_{sp}$) the classical dynamics on the hypersphere is near regular; see Figs. 2(a)–2(c). This is a consequence of the reduction of α motion in this case to small regions around potential wells at $\alpha = 0$ and $\pi/2$, where the individual motions of two electrons are less correlated. In the range $\epsilon_{sp} < \epsilon < 0.261$ the two-electron dynamics is mixed and the Poincaré sections show the typical structure with regular islands embedded into chaotic areas [Figs. 2(d)–2(h)]. With increase in the scaled energy the motion becomes more chaotic and, for positive energies, it becomes essentially ergodic [Fig. 2(i)].

C. The collinear configurations

For collinear configurations the mutual angle between the electrons is either $\vartheta = 0$ or $\vartheta = \pi$ with $p_\vartheta = 0$ (in both cases). In the first case the electrons reside on the same side of the nucleus (the *Zee* configuration), whereas in the second case they are on opposite sides (the *eZe* configuration). Since we consider constrained dynamics with fixed hyperradius (the motion on the hypersphere), both configurations have only one degree of freedom, along the α coordinate, and the corresponding 1D Hamiltonian function reads

$$h(p_\alpha,\alpha) = \tfrac{1}{2}p_\alpha^2 + C(\alpha), \tag{8}$$

where

$$C(\alpha) = -\frac{Z}{\cos\alpha} - \frac{Z}{\sin\alpha} + \frac{1}{|\cos\alpha \pm \sin\alpha|}. \tag{9}$$

The signs "−" and "+" correspond to the cases $\vartheta = 0$ and π, respectively. This Hamiltonian function describes in fact the constrained ($R = \text{const}$) two-electron dynamics in the 1D invariant subspaces (ii) and (iii) (see Sec. II A).

For a given scaled energy, each configuration (*Zee* or *eZe*) in the corresponding 1D configuration space reduces to a single PO. For the *Zee* configuration this is the frozen planet PO, whereas for the *eZe* configuration the corresponding orbit is the inverted frozen planet PO if $\epsilon < \epsilon_{sp}$ and the asymmetric stretch PO if $\epsilon > \epsilon_{sp}$ (see Fig. 1). The corresponding phase trajectories $p_\alpha(\alpha) = \pm\sqrt{2[\epsilon - C(\alpha)]}$ for different scaled energies are shown in Fig. 4. Examples of these POs in real space for two values of the scaled energy ($\epsilon < \epsilon_{sp}$ and $\epsilon > \epsilon_{sp}$) are shown in Fig. 5.

Information about the stability of the POs can be obtained by analyzing the fixed points in Poincaré sections or by calculating the corresponding Lyapunov exponents [27]. Figure 6 shows the Lyapunov exponents λ for the short POs for $Z = 2$ as functions of the scaled energy. It can be seen that the FP orbit is stable ($\lambda = 0$) in the interval $-6.283 < \epsilon < -2.972$. By inspecting the Poincaré sections (6) at different scaled energies, we find that the stable FP PO bifurcates at the ends of this interval. Except for the change of stability of the FP orbit, the bifurcations result in the appearance of new POs represented by elliptic fixed points located near the fixed points related to the FP PO (see Fig. 2). These new orbits are essentially off collinear (planetary orbits). In contrast to the FP orbit, the IFP orbit is always stable ($\lambda = 0$ for all $\epsilon < \epsilon_{sp}$; see Fig. 6). This is not true for the other type of PO belonging to the *eZe* configuration, i.e., for the AS PO. Examinations of the Poincaré sections (7) show that the AS orbit is stable for $\epsilon \in (\epsilon_{sp}, \epsilon_{bif})$, where $\epsilon_{bif} = -3.487$ (for $Z = 2$). At the scaled energy $\epsilon = \epsilon_{bif}$ the orbit bifurcates to an unstable AS and a stable ASC orbit [these two orbits at $\epsilon = -3.3$ are shown in Figs. 7(a) and 7(b), respectively].

Recall that the stability of a trajectory is defined with respect to small deviations in directions which are perpendicular to the motion along the trajectory. Since the system we study has two degrees of freedom and the corresponding collinear configurations have only one, along the α coordinate, stability of a collinear PO essentially means that this orbit is stable with respect to deviations in the ϑ direction. Consequently, a stable collinear PO is surrounded by an island of stability in phase space containing off-collinear orbits with the same kinematics in the α direction as in the collinear orbit. Thus,

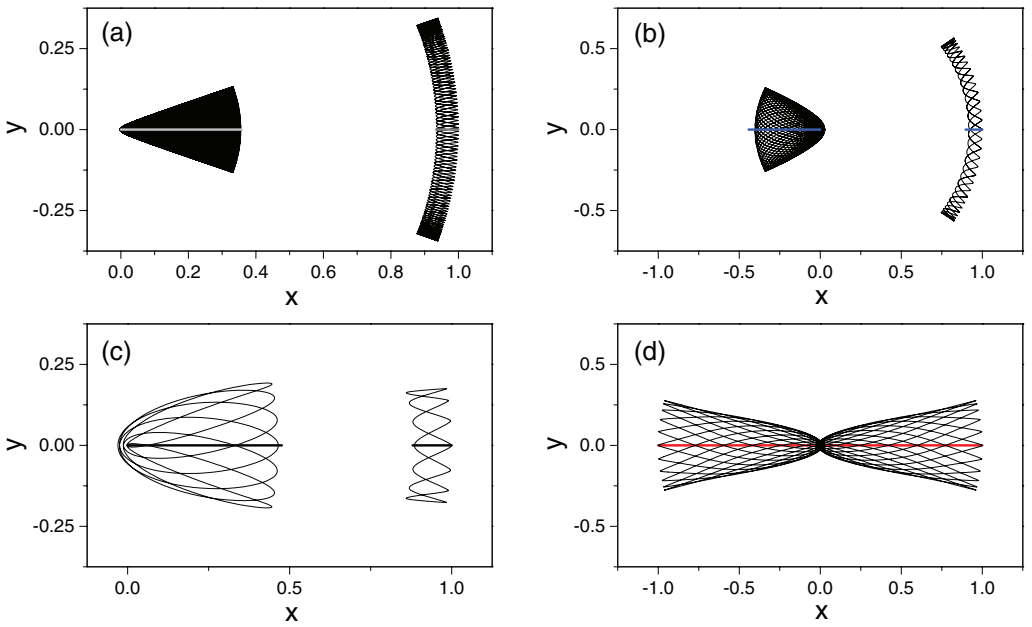

FIG. 5. (Color online) The collinear *Zee* (left) and *eZe* (right) POs for $R = 1$ and two values of the scaled energy, $\epsilon = -6$ (top) and $\epsilon = -4$ (bottom), shown in real space (straight colored lines show the electron paths): (a) the FP PO, (b) the IFP PO, (c) the FP PO, and (d) the AS PO; as well as off-collinear orbits (black lines) in their vicinities. The nucleus ($Z = 2$) is located at the origin of the coordinate system. Note that the collinear orbits shown here correspond to the phase trajectories drawn with arrows in Fig. 4.

the definition of collinear configuration can be extended to the set of all stable trajectories (including the off-collinear ones) surrounding the fundamental collinear PO. Examples of such off-collinear orbits belonging to the extended *Zee* and *eZe* configurations are shown in Fig. 5. Note that the orbits in the neighborhood of stable FP POs are very similar to the related orbits for the unconstrained two-electron system [23]. The orbits belonging to the constrained and the unconstrained dynamics, however, may be very different in stability. As we can see from Fig. 6, for the motion on the hypersphere the stability of POs depends on the scaled energy, whereas in the full phase space the FP PO is always stable and the AS PO is always unstable [20,26]. The IFP configuration [Fig. 5(b)], as

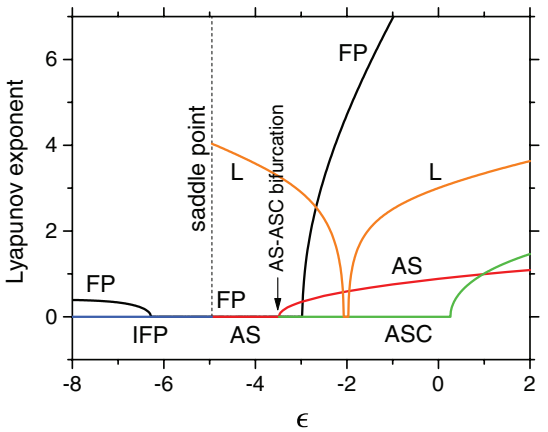

FIG. 6. (Color online) The Lyapunov exponents as functions of the scaled energy for the FP (black), IFP (blue), AS (red), ASC (green), and L (orange) POs ($Z = 2$) at fixed hyperradius.

we have mentioned above, does not exist in the case of the full dynamics.

D. The asynchronous configuration

Out-of-phase planar models for the helium atom (in the full configuration space) were analyzed several times in the last century in order to describe semiclassically the ground or symmetrically exited states with $L = 0$ [24,28,29] (see also Figs. 3 and 4 and the related text in Ref. [14]). In the simplest of such models [24] two electrons move around the nucleus asynchronously (with a phase shift of half a period), one clockwise and the other counterclockwise (when $L = 0$), on two equivalent perturbed Kepler ellipses with major axes oriented in opposite directions. Thus, when one electron passes through the perihelion, the second is at its aphelion. A subsequent analysis of the model [29], however, has revealed that such a simple (short) PO does not exist for fully correlated electrons (except in the collinear limit—the AS PO). In fact, due to the mutual electron interaction and the out-of-phase kinematics, the asynchronous configuration has an additional degree of freedom—slow oscillations of the angle Θ between the major axes of single electron orbits (bending vibrations around the equilibrium value $\Theta = \pi$) [19,28].

In contrast to the full (unconstrained) two-electron dynamics, the asynchronous periodic orbit (the ASC PO), which is kinematically equivalent to the model proposed in Ref. [24] ($\Theta = \pi$ all the time), is dynamically allowed in the case of motion on the hypersphere for $\epsilon > \epsilon_{\rm bif}$; see Figs. 7(a) and 7(b). This fundamental PO is in the Poincaré sections in Figs. 2(e)–2(h), 3(c), and 3(d) represented by elliptic fixed points (green dots), which are located symmetrically below

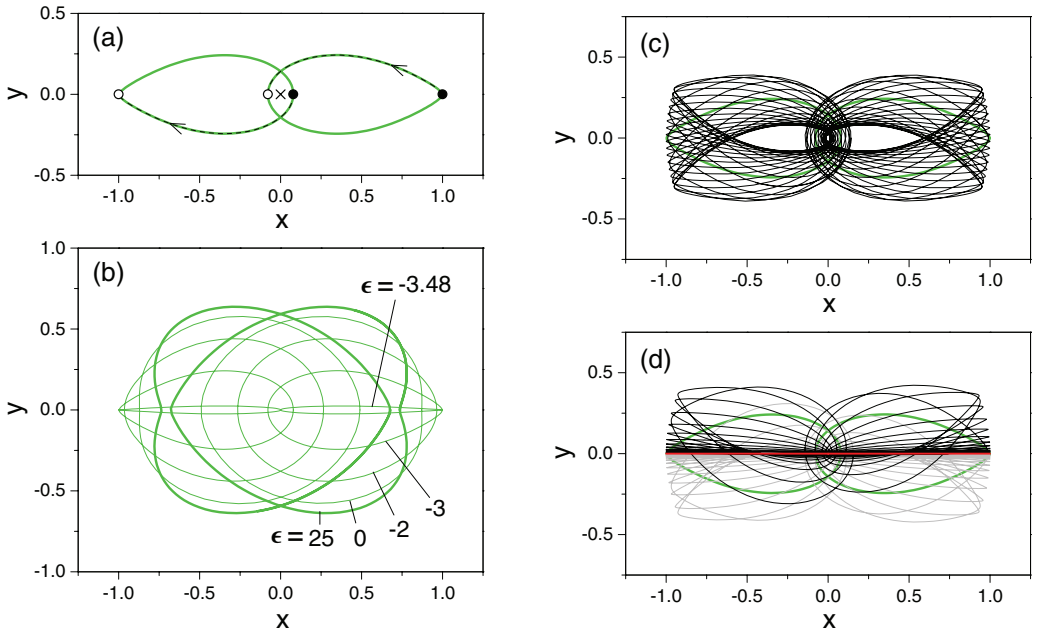

FIG. 7. (Color online) (a) The asynchronous (ASC) PO for $\epsilon = -3$. The full circles mark the positions of two electrons while they pass from the same side of the nucleus (cross) through the collinear arrangement. The open circles mark their positions after half a period. (b) The ASC POs for $\epsilon = -3.48, -3, -2$, 0, and 25. (c) and (d) Trajectories in the neighborhood of the ASC PO for $\epsilon = -3$ with different amplitudes of the perpendicular component of motion. The first one (c), with smaller amplitude, is stable. The second one (d) approaches asymptotically the (unstable) AS collinear configuration (red line). To show this process transparently a part of the trajectory is drawn in a lighter color.

and above the centers of sections. For scaled energies just above the bifurcation point the orbit is very close to the AS PO, but for higher values of ϵ it becomes essentially off collinear [see Fig. 7(b)]. One can see from Fig. 6 that the ASC PO is stable in the interval $\epsilon_{\rm bif} < \epsilon < 0.261$. Actually, at higher scaled energies the only stable configuration is just the asynchronous one and the latest stable orbit which survives before the system becomes ergodic is the ASC PO (see Fig. 2). The increasing instability of the ASC PO with the scaled energy can be explained by the decreasing distance between electrons (and thus the increasing Coulomb repulsion) at the points of their closest approach, which occurs at $\vartheta = 0$ [see the "double-heart" orbit in Fig. 7(b)].

The trajectories surrounding the ASC PO (represented by closed curves around the green dots in the Poincaré sections in Figs. 2 and 3) have, in addition to the fundamental asynchronous mode, also a perpendicular component of motion leading to slow oscillations of the angle Θ (bending vibrations). Examples of such trajectories for $\epsilon = -3$, with different amplitudes of the perpendicular component, are shown in Figs. 7(c) and 7(d). The first one (c) has smaller amplitude and it is stable. In the second case (d) the amplitude is so large that the trajectory, which is initially close to the asynchronous configuration, approaches asymptotically the AS collinear configuration (red line). This trajectory corresponds to the separatrix shown in the Poincaré section in Fig. 3(d) (red curve). The hyperbolic fixed point in this separatrix is related to the AS PO which is for $\epsilon = -3$ unstable. Thus, the trajectory in Fig. 7(d) can be obtained also from the AS PO by introducing a very small perpendicular deviation. The trajectories with amplitudes of the perpendicular component which are larger than that for the trajectory in Fig. 7(d) are located outside the phase-space area restricted by the separatrix, but this motion can still be stable (see Fig. 3).

E. The Langmuir configuration

As we have seen in Sec. II A, the constrained motion ($R = \text{const}$) of two electrons on the Wannier ridge ($r_1 = r_2$) belongs to a 1D invariant subspace [marked by (i)] of the 2D configuration space. The only degree of freedom here can be described by the angle ϑ. Moreover, due to the electrostatic repulsion between electrons, this motion reduces to pure bending vibrations around the equilibrium value $\vartheta = \pi$. The corresponding trajectory is essentially the counterpart of the Langmuir oscillatory PO for the unconstrained system [25]. These motions are, however, different in many features, for example, in the amplitude of the bending vibrations, which in the constrained case depends on the scaled energy. Further, in this case the electron paths lie on the common circle $r_1 = r_2 = R/\sqrt{2}$ [see Fig. 8(a)], which is not the case for the unconstrained motion.

The motion in the 1D invariant subspace (i) can be described by the Hamiltonian function (5) if we put $\alpha = \pi/4$ and $p_\alpha = 0$, i.e., by $h(p_\vartheta, \vartheta) = 2p_\vartheta^2 - 2\sqrt{2}\,Z + 1/\sqrt{2}\sin(\vartheta/2)$. It is convenient here to introduce the new variable $\chi = (\pi - \vartheta)/2$. The appropriate Hamiltonian function then has the form

$$h(p_\chi, \chi) = \frac{p_\chi^2}{2} + \frac{\sec\chi - 4Z}{\sqrt{2}}. \tag{10}$$

The minimal value of the scaled energy ϵ for which the configuration exists is $\epsilon_{\rm sp}$. Then $\chi = 0$ and $p_\chi = 0$ ($\vartheta = \pi$ and $p_\vartheta = 0$), i.e., the electrons are at rest at the opposite sides of the nucleus [see Fig. 8(a)]. By increasing the scaled energy the

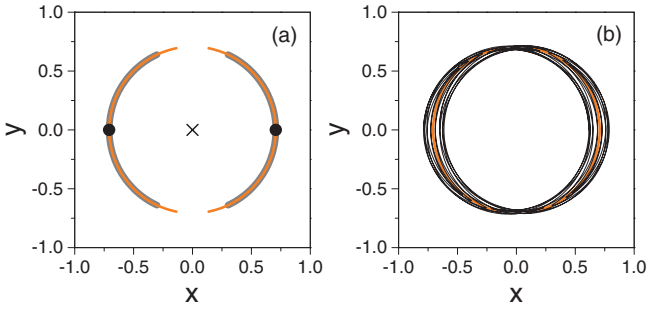

FIG. 8. (Color online) (a) The Langmuir PO ($R = 1$) for $Z = 2$ at $\epsilon = -2$ (orange lines), $\epsilon = -4$ (thick gray lines), and $\epsilon = \epsilon_{sp}$ (black circles). (b) A stable trajectory in the vicinity of the Langmuir PO for $\epsilon = -2$.

amplitude of bending vibrations χ_0 increases. Its value follows from the condition $p_\chi = 0$ which determines the positions of the vibration turning points $\pm\chi_0$. Using Eq. (10) one obtains

$$\chi_0 = \arccos(\sqrt{2}\epsilon + 4Z)^{-1}. \tag{11}$$

As mentioned above, the Langmuir PO is in Poincaré section (6) represented by the fixed point located at $(\alpha, p_\alpha) = (\pi/4, 0)$. For $Z = 2$ and for the scaled energy $\epsilon = -2$ this point is the elliptic fixed point [see Fig. 2(f)]. By calculating the Lyapunov exponent for this orbit at different scaled energies (see Fig. 6) it is found that for $Z = 2$ the orbit is stable only in the narrow interval $\epsilon \in (-2.072, -1.969)$. A stable trajectory in the vicinity of the Langmuir PO for $\epsilon = -2$ is shown in Fig. 8(b).

III. ADIABATIC LINES RELATED TO FUNDAMENTAL PERIODIC ORBITS

A. Quantization procedure

Just as the hyperspherical adiabatic energies are determined by solving the hyperspherical adiabatic eigenvalue problem (the Schrödinger equation for fixed values of the hyperradius R), in principle one can obtain semiclassical adiabatic energies by quantizing the classical two-electron motion on the hypersphere. A semiclassical calculation of adiabatic (electronic) energies has been done successfully for the two-Coulomb-center problem (the H_2^+ system) [30] which is separable in ellipsoidal coordinates. In the case of two-electron atomic systems, however, the (2D) motion on the hypersphere is neither fully regular nor chaotic but mixed and, for this reason, the calculation of semiclassical adiabatic energies is not a trivial task. On the other hand, the main idea of this paper is to analyze some properties of the quantum-mechanically determined adiabatic curves using classical dynamics as a tool. For this analysis it may be sufficient to consider the most important classical configurations studied in the previous section. We have seen that these configurations, except the asynchronous one, are related to 1D invariant subspaces of the 2D configuration space. The corresponding 1D motions can be simply quantized by the use of WKB rules. Semiclassical adiabatic curves obtained in this way are essentially related to short (fundamental) POs which represent these configurations. Within this framework short POs are treated as fundamental modes of the two-electron motion on the hypersphere and the quantization is performed by taking into account only the degree of freedom along the corresponding trajectory. The calculation of adiabatic curves associated with fundamental modes then can be extended to the configurations which are not necessarily related to 1D invariant subspaces, for example to the asynchronous configuration. In order to make a difference between the adiabatic curves which are solutions of the full (2D) hyperspherical adiabatic eigenvalue problem and those which are related to a given PO (which are essentially solutions of the 1D eigenvalue problem for the corresponding mode), the latter will be referred to as the *adiabatic lines* related to a PO or simply the "PO lines."

The first step in determining these lines is to calculate the scaled actions along the (five) fundamental POs as functions of the scaled energy. Before we turn to the calculation, recall that the symmetry of the Hamiltonian function under the exchange of electronic coordinates allows the reduction of the configuration space to the fundamental domain $\alpha \in [0, \pi/4]$, i.e., to the desymmetrized region with $r_1 \geqslant r_2$. Formally, it can be constructed by introducing an elastically reflecting wall at the Wannier ridge ($r_1 = r_2$). Since all information about the motion, either classical or quantum mechanical, is contained in the fundamental domain, the scaled actions we shall use to quantize the classical motion will be given by the integral

$$s = \oint_{\mathrm{PO}^*} (p_\alpha \, d\alpha + p_\vartheta \, d\vartheta), \tag{12}$$

where PO* denotes the path of a given PO in the fundamental domain. In order to get the function $s(\epsilon)$ for this PO, the integral (12) must be calculated along the paths PO* at different scaled energies ϵ. These functions for the five fundamental POs in an interval of scaled energies around ϵ_{sp} are shown in Fig. 9.

When the function $s(\epsilon)$ for a given PO is determined, one can obtain the corresponding semiclassical energies using scaling relations and the WKB quantization condition

$$S = 2\pi n + \phi, \quad n = 0, 1, 2, \ldots, \tag{13}$$

where n is the nodal quantum number along the path PO* (here we use atomic units where $\hbar = 1$). The phase shift ϕ depends on the number and type of turning points along the path PO*, as well as on the symmetry of the corresponding quantum state. The latter is a consequence of the reduction of

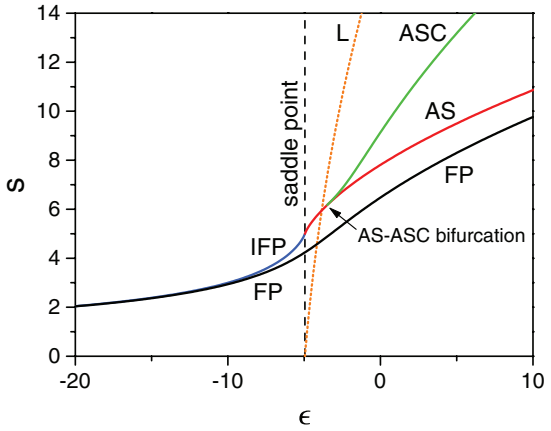

FIG. 9. (Color online) Scaled actions for the five fundamental POs as functions of the scaled energy.

the configuration space to the fundamental domain. Namely, in the full configuration space the symmetric two-electron wave functions (singlet states) have an antinode at the Wannier ridge ($\alpha = \pi/4$), whereas the antisymmetric ones (triplet states) have a node there. In the fundamental domain, however, the value of the wave function at $\alpha = \pi/4$ is treated as a boundary condition and, in the case of triplet states, the node at the Wannier ridge is not included in the quantization condition (13). For the POs which cross the Wannier ridge this fact leads to a phase loss of π when the quantization is performed in the fundamental domain, which must be compensated by an additional phase shift of π (for triplet states) in the total shift ϕ. The values of ϕ for particular POs will be estimated below.

Using the first and the third of relations (4), the semiclassical adiabatic energy as a function of the hyperradius, i.e., the adiabatic line $E_n(R)$, can be given in the parametric form

$$R(\epsilon) = \left(\frac{S}{s}\right)^2 = \left[\frac{2\pi n + \phi}{s(\epsilon)}\right]^2, \quad E_n(\epsilon) = \frac{\epsilon}{R(\epsilon)}. \tag{14}$$

Note that, since $s(\epsilon)$ is an increasing function for all five fundamental POs (see Fig. 9), high values of the scaled energies in an adiabatic line correspond to small values of R. Alternatively, if the inverse function $\epsilon(s)$ can be evaluated, using the same scaling properties and the quantization condition (13), one has explicitly

$$E_n(R) = \frac{1}{R}\,\epsilon[(2\pi n + \phi)/\sqrt{R}]. \tag{15}$$

One can see from expression (15) that $E_n(R)$, like the adiabatic energies in quantum-mechanical calculations, diverge when $R \to 0$. Thus, at small values of the hyperradius it is more convenient, instead of $E_n(R)$, to consider the so-called adiabatic potentials

$$U_n(R) = -2R^2 E_n(R), \tag{16}$$

which take finite values for $R \to 0$.

In the other limit when $R \to \infty$ one has $s \to 0$ [see Eq. (4)] and $\epsilon \to -\infty$ (see Fig. 9). In this case there are only two fundamental POs, the FP and the IFP POs. Generally, the two-electron motion in this limit is localized around one of the singularities of the potential (2), i.e., around $\alpha = 0$ or $\alpha = \pi/2$, and the Hamiltonian function (3) can be approximated by $H_R = [\frac{1}{2}(P_\alpha^2 + P_\vartheta^2/\alpha^2) - ZR/\alpha]/R^2$. The expression in the square brackets is equivalent to the Hamiltonian of a one-electron atom with the eigenenergies $-(ZR)^2/2N^2$ ($N = 1,2,3,\ldots$). Thus in the limit $R \to \infty$ it is $E(R) \to -Z^2/2N^2$, i.e., the adiabatic energies related to FP and IFP POs, as well as those which are solutions of the full (2D) adiabatic eigenvalue problem, converge to the well-known ionization thresholds of two-electron atoms determined by the principal quantum number N of the inner electron. For this reason in the range $E(R) < 0$ (large R) it is convenient to plot the adiabatic energies as effective quantum numbers

$$N_{\rm eff}(R) = Z/\sqrt{-2E(R)}, \tag{17}$$

which in the limit $R \to \infty$ converge to the corresponding values of the quantum number N.

Since the adiabatic energy lines $E_n(R)$ related to the FP and IFP POs converge to the ionization threshold with $N = n + 1$, the nodal quantum number n and the principal quantum number N are in this way directly related. Moreover, this relation can be extended to the AS and ASC adiabatic lines, because they are continuously connected with the IFP line with the same n. These facts are essentially consequences of the analogous relationship between the corresponding scaled actions (see Fig. 9).

B. Collinear configurations

For the collinear configurations, both the *eZe* and the *Zee*, we have $p_\vartheta = 0$ and $p_\alpha = \pm\sqrt{2[\epsilon - C(\alpha)]}$ [from the Hamiltonian function (8)], where $C(\alpha)$ is given by Eq. (9). Then the scaled action (12) reduces to

$$s = \oint_{\rm PO^*} p_\alpha\, d\alpha = 2\int_0^{\alpha_0} |p_\alpha|\, d\alpha = 2\sqrt{2}\int_0^{\alpha_0} \sqrt{\epsilon - C(\alpha)}\, d\alpha, \tag{18}$$

where

$$\alpha_0 = \begin{cases} \alpha_{\rm tp} & \text{if} \quad \epsilon < C(\pi/4), \\ \pi/4 & \text{if} \quad \epsilon \geqslant C(\pi/4). \end{cases} \tag{19}$$

The position of the turning point $\alpha_{\rm tp}$ can be determined from the condition $p_\alpha = 0$, i.e., it is the solution of the equation $C(\alpha) = \epsilon$ within the interval $(0,\pi/4)$. Note that for the *Zee* configuration $C(\pi/4) \to +\infty$ and in this case (i.e., for the FP POs) $\alpha_0 = \alpha_{\rm tp}$ for all ϵ. For the *eZe* configuration, however, $C(\pi/4) = \epsilon_{\rm sp}$ and $\alpha_0 = \alpha_{\rm tp}$ for the IFP POs whereas $\alpha_0 = \pi/4$ for the AS POs. The actions $s(\epsilon)$ for the fundamental POs belonging to the collinear configurations (the FP, IFP, and AS POs) in an interval of scaled energies around $\epsilon_{\rm sp}$ are shown in Fig. 9.

Another quantity necessary for determining the adiabatic energies corresponding to a given PO is the phase shift ϕ. It includes the contributions of two (generalized) turning points which are in the case of collinear configurations located at $\alpha = 0$ and $\alpha = \alpha_0$ [see Figs. 10(a) and 10(b)], The first turning point is in fact the Coulomb singularity and the corresponding phase shift is $\phi_1 = 3\pi/2$. The second one is for the FP and IFP orbits located at $\alpha = \alpha_{\rm tp}$ where the potential has a finite slope (regular turning point) and the phase shift is $\phi_2 = \pi/2$. For the AS PO, however, the second turning point is on the Wannier ridge, which in the fundamental domain behaves as an elastically reflecting wall, and the corresponding phase shift is zero ($\phi_2 = 0$). The total phase shift ($\phi = \phi_1 + \phi_2$) is therefore $\phi = 2\pi$ for the FP and IFP POs and $\phi = 3\pi/2$ for the AS PO. For very high scaled energies ($\epsilon \to +\infty$), however, the Coulomb singularities behave as rigid walls and the corresponding phase shifts are $\phi = \pi$ ($\phi_1 = \pi$, $\phi_2 = 0$) for the *eZe* configuration and $\phi = 2\pi$ ($\phi_1 = \phi_2 = \pi$) for the *Zee* configuration [see Figs. 10(a) and 10(b)]. The estimated values of ϕ for the AS PO are, however, correct only for the spatially symmetric (singlet) two-electron states. Namely, since this PO crosses the Wannier ridge, the total phase shift ϕ for antisymmetric (triplet) states must be increased by π [see the discussion below Eq. (13)]. On the other hand, the FP and IFP POs do not cross the Wannier ridge and there is no additional phase shift for triplet states.

The adiabatic energies $E_n(R)$ for symmetric states with $n = 1$, 2, and 3 of helium ($Z = 2$) which correspond to the FP, IFP, and AS POs are shown in Fig. 11(a) (thick colored lines)

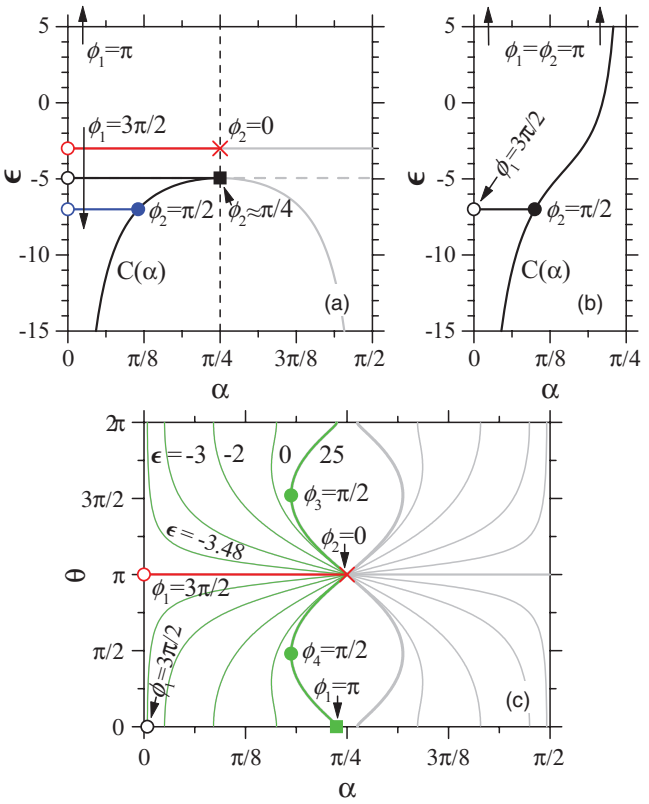

FIG. 10. (Color online) (a) Characteristic trajectories of the collinear *eZe* configuration shown in the fundamental domain: the IFP PO ($\epsilon = -7$, blue line), separatrix ($\epsilon = \epsilon_{sp}$, black line), and AS PO ($\epsilon = -3$, red line). (b) An example of a trajectory belonging to the collinear *Zee* configuration (the FP PO) shown in the fundamental domain ($\epsilon = -7$, black line). The turning points ($i = 1,2$) for each orbit are labeled by the related phase shift ϕ_i. (c) The AS PO (red line) and several ASC POs ($\epsilon = -3.48, -3, -2, 0, 25$, green lines) shown in the fundamental domain of (α,ϑ) space. The turning points for the AS and the ASC POs with $\epsilon = -3.48$ and 25 are labeled by the related phase shifts.

together with the quantum-mechanically calculated energies $E_n^{(\mathrm{qm})}(R)$ for the collinear (*Zee* and *eZe*) configurations (thick gray lines). The energies $E_n^{(\mathrm{qm})}(R)$ are the eigenvalues of the 1D Hamiltonian

$$\hat{H}_R = -\frac{1}{2R^2}\frac{d^2}{d\alpha^2} + \frac{C(\alpha)}{R}, \tag{20}$$

which corresponds to the Hamiltonian function (3) when $P_\vartheta = 0$ and $\vartheta = 0$ or π. Emphasize that the eigenenergies $E_n^{(\mathrm{qm})}(R)$ differ by the term $1/8R^2$ from the adiabatic energies $\mathcal{E}_n(R)$, introduced in the quantum mechanical treatment of the collinear helium atom in hyperspherical coordinates [31], due to the same difference in the corresponding Hamiltonians [compare Eq. (6) in Ref. [31] and Eq. (20)]. The behavior at small values of the hyperradius, which are related to high values of (scaled) energies, are better visible if we consider the adiabatic potentials (16) [see Fig. 11(b)]. A difference between the quantum-mechanical and the semiclassical adiabatic lines is a consequence of the approximate character of the values introduced above for the phase shift ϕ when these values are used in a wide range of scaled energies. In addition, if we use different values of ϕ in different intervals of the scaled energy, as in the case of the *eZe* configuration, then the semiclassical lines become discontinuous at the interval edges. Such a behavior is typical when the energy becomes equal to the potential barrier maximum ($\epsilon = \epsilon_{sp}$ for the *eZe* configuration). The exact phase shift, therefore, should be a smooth function of the scaled energy ϵ (or the hyperradius R). The WKB quantization using such a parameter-dependent phase shift, instead of one (or several) fixed value(s), is known as the uniform semiclassical quantization (for H_2^+ see Ref. [30]) The exact phase shift can be determined by comparing the semiclassical and the corresponding quantum-mechanical solutions, for example by fitting the semiclassical wave function to the exact quantum-mechanical one in the range which is far from turning points (see, e.g., Ref. [32]). Alternatively, this shift (for given n and R) can be extracted from the condition (13) if we calculate the action integral $S(E)$ at the corresponding (previously determined) quantum-mechanical energies $E_n^{(\mathrm{qm})}(R)$, i.e., $\phi_n(R) = S(E_n^{(\mathrm{qm})}(R)) - 2\pi n$. Note that in this case $E_n^{(\mathrm{WKB})}(R) \equiv E_n^{(\mathrm{qm})}(R)$. Then, instead of performing a uniform semiclassical quantization in order to get the exact adiabatic energies related to a given PO, we can simply use the eigenenergies of the Hamiltonian (20) in the corresponding invariant subspace.

C. The asynchronous configuration

The action along the ASC PO, in contrast to the collinear POs, cannot be calculated before computing the orbit itself. When the orbit is determined, i.e., when we know how the phase point $(\alpha,\vartheta,P_\alpha,P_\vartheta)$ evolves in time, the action along the orbit in the fundamental domain can be calculated as

$$S = \frac{1}{2R^2}\int_0^{\mathcal{T}} \left(P_\alpha^2 + \frac{P_\vartheta^2}{\sin^2\alpha\cos^2\alpha}\right) dt, \tag{21}$$

where $\mathcal{T}$ is the period of the full orbit. In order to get the function $s(\epsilon)$ a series of the ASC orbits for $R = 1$ and different values of the scaled energy ϵ [then $s(\epsilon) = S(E)$] is calculated using the monodromy method [27]. A part of this function (for lower scaled energies) is shown in Fig. 9.

Since the AS PO and the ASC PO coincide at $\epsilon = \epsilon_{bif}$ (the bifurcation point), for the WKB quantization of the latest orbit at lower energies ($\epsilon < 0$) we shall use the same phase shift as for the AS PO, i.e., for singlet states $\phi = 3\pi/2$ [$\phi_1 = 3\pi/2$, $\phi_2 = 0$; see Fig. 10(c)]. At higher energies, however, two new turning points appear [see the double-heart configuration in Figs. 7 and 10(c)] and the total phase shift is $\phi = \sum_{i=1}^4 \phi_i$. At very high scaled energies the first turning point becomes very close to the Coulomb singularity at $(\alpha,\vartheta) = (\pi/4,0)$, which behaves as a rigid wall. Thus, in the limit $\epsilon \to +\infty$ one has $\phi = 2\pi$ ($\phi_1 = \pi$, $\phi_2 = 0$, $\phi_3 = \phi_4 = \pi/2$) and we shall use this value for small R. For triplet states the phase shift must be additionally increased by π. Unfortunately, for the ASC configuration it is not possible to find easily the quantum-mechanical eigenenergies and perform a uniform semiclassical quantization. For this reason in the forthcoming analysis we shall consider the semiclassical adiabatic energies and potentials obtained using the phase shifts for the limiting cases [see Fig. 11(b)].

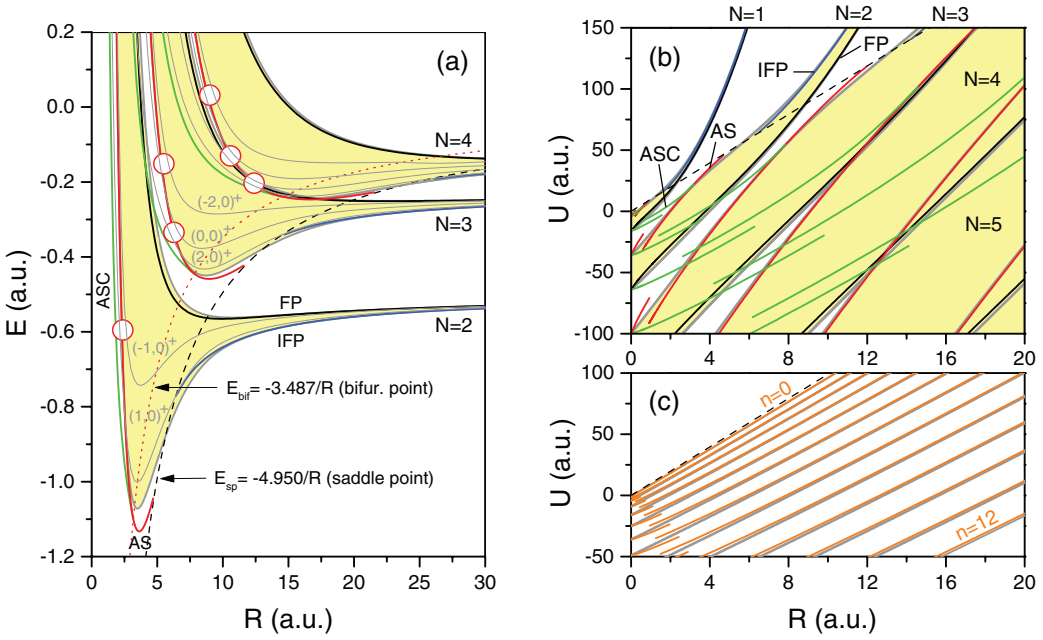

FIG. 11. (Color online) The adiabatic lines for symmetric states (with $L = 0$) of helium ($Z = 2$) related to fundamental POs calculated semiclassically (FP, black lines; IFP, blue lines; AS, red lines; ASC, green lines; and L, orange lines) and quantum-mechanically (thick gray lines): (a) adiabatic energies $E_n(R)$ ($n = 1,2,3$) related to the FP, IFP, AS, and ASC POs; (b) adiabatic potentials $U_n(R)$ related to the FP, IFP, AS, and ASC POs; and (c) adiabatic potentials $U_n(R)$ related to the L PO. The saddle and bifurcation point energies (potentials) are drawn by dashed and dotted lines, respectively. The areas bounded by the adiabatic lines related to the collinear (*eZe* and *Zee*) configurations, converging for each area to the same (Nth) ionization threshold, are highlighted (yellow). For comparison the adiabatic energies $E_\mu(R)$ [$\mu = (K,T)^A_N$] which are solutions of the full (2D) quantum-mechanical problem (adiabatic curves) are shown in (a) (thin gray lines). The red circles mark the positions of anticrossings of the adiabatic curves.

D. The Langmuir configuration

As we have seen in Sec. II, the constrained ($R = \text{const}$) two-electron motion on the Wannier ridge ($\alpha = \pi/4$) when $L = 0$ reduces to oscillations of the angle ϑ (or χ), which we call, in analogy with the unconstrained motion, the Langmuir orbits, and can be described by the Hamiltonian function (10). Then, for a given scaled energy ϵ, one has $p_\chi = \pm 2^{1/4}[\sqrt{2}\epsilon + 4Z - \sec\chi]^{1/2}$ and the action integral along the corresponding orbit is

$$s = \oint p_\chi \, d\chi = 4\int_0^{\chi_0} |p_\chi| \, d\chi = 2^{9/4}\int_0^{\chi_0} \sqrt{\sec\chi_0 - \sec\chi}\, d\chi, \tag{22}$$

where $\pm\chi_0$ are the turning points given by Eq. (11).

At lower energies ($\epsilon \sim \epsilon_{sp}$) the potential in the Hamiltonian function (10) is nearly parabolic and the phase shifts at $\pm\chi_0$ are $\phi_1 = \phi_2 = \pi/2$. For high energies ($\epsilon \to +\infty$), however, the turning points are close to the ends of the χ domain $(-\pi/2,\pi/2)$, where the potential behaves like a rigid wall, and $\phi_1 = \phi_2 = \pi$. Therefore, the phase shift in the WKB quantization condition (13) will be $\phi = \pi$ for small energies (large R) and $\phi = 2\pi$ for high energies (small R). Since the Langmuir PO does not have a component of motion in the α direction, in this case there is no difference in the phase shift between singlet and triplet states. The corresponding potential lines $U_n(R)$ are shown in Fig. 11(c) (orange lines) together with those obtained quantum mechanically (gray lines).

In the quantum-mechanical treatment the adiabatic energies related to the Langmuir PO are the eigenvalues of the 1D Hamiltonian

$$\hat{H}_R = -\frac{1}{2R^2}\frac{d^2}{d\chi^2} + \frac{\sec\chi - 4Z}{\sqrt{2}R}. \tag{23}$$

We have solved the corresponding Schrödinger equation $\hat{H}_R\psi_n(\chi;R) = E_n(R)\psi_n(\chi;R)$ numerically using methods similar to those described in Ref. [31]. This equation, however, in the limit $R \to 0$ reduces to $d^2\psi_n/d\chi^2 = U_n(0)\psi_n$, which can be solved analytically. Namely, if we formally treat $-U_n(0)/2$ as eigenenergies, the latter equation is equivalent to the Schrödinger equation for a particle in a one-dimensional infinite square well of width π, whose eigenenergies are $(n+1)^2/2$. Therefore, we have

$$U_n(0) = -(n+1)^2. \tag{24}$$

IV. ANALYSIS OF THE ADIABATIC CURVES

A. Localization of multiplets of adiabatic curves

In a recent quantum-mechanical analysis [31] it has been shown that a set of $^1S^e$ (singlet, $L = 0$) adiabatic curves of helium which converge to the same ionization threshold (the curves with the same N but different K—the Nth multiplet) is, for sufficiently large R, confined in the area limited from the bottom and from the top by the adiabatic lines related to the collinear (*eZe* and *Zee*) configurations which also converge to this (Nth) ionization threshold. These (*eZe*,*Zee*) areas for

$N = 2$, 3, and 4 are shown in Fig. 11(a) as yellow zones delimited by thick gray lines (*eZe* and *Zee* lines). The thin gray lines in the same figure are the adiabatic curves $E_\mu(R)$ $[\mu = (K,0)^+_N;\ K = -N+1, -N+3, \ldots, N-1;$ $N = 2,3,4]$. The curves of a given (Nth) multiplet which are the closest to the *eZe* (*Zee*) (limiting) lines are those which correspond to the minimal (maximal) bending excitations ($K = N-1$ and $K = -N+1$), respectively. These features are confirmed by the present semiclassical analysis—the multiplets are delimited from the bottom and from the top by the adiabatic lines related to the IFP or AS and FP POs [blue or red and black lines in Fig. 11(a)], respectively. Here the lower limiting line of a given multiplet is related to the IFP PO in the range $E(R) < E_{\rm sp}(R)$ and to the AS PO in the range $E_{\rm sp}(R) < E(R) < E_{\rm bif}(R) = -3.487/R$ [the area between the dashed and the red dotted lines in Fig. 11(a)] where the AS orbit is stable.

At smaller values of R, however, the adiabatic curves of a given multiplet cross the lower (*eZe*) limiting line and leave the corresponding yellow area. One can see from Fig. 11(a) that these crossings occur in the domain $E(R) > E_{\rm bif}(R)$ [above the bifurcation (red dotted) line] where the AS PO is unstable. With further decrease in R, the lowest-energy curve ($K = N-1$) of a given (Nth) multiplet approaches the adiabatic line related to the ASC PO (green line with $n = N-1$), whereas the highest one ($K = -N+1$) approaches the corresponding AS line (red line with $n = N-1$). In other words, the Nth multiplet, which is at large values of the hyperradius localized in the (*eZe*,*Zee*) area [which can also be called the (IFP-AS,FP) area] with $n = N-1$, at small R moves to the (ASC,AS) area characterized by the same n (see Fig. 12). Finally, in the limit $R \to 0$ the adiabatic energies diverge but the corresponding adiabatic potentials [thin black lines in Fig. 13(a)] converge to the 1D square-well values given by Eq. (11) in Ref. [31].

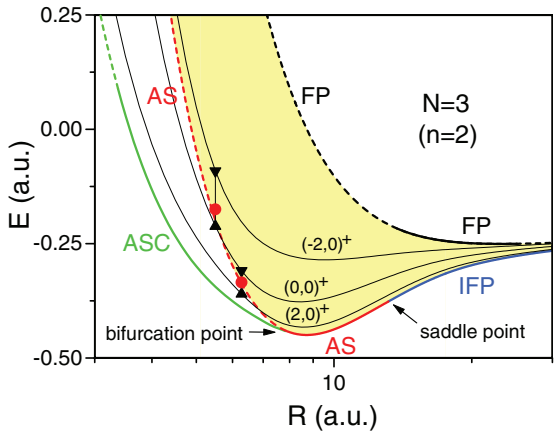

FIG. 12. (Color online) The adiabatic curves of helium ($Z = 2$) with $L = 0$ (thin black lines) which converge to the third ionization threshold ($N = 3$) and the corresponding (quantum-mechanically calculated) adiabatic lines ($n = 2$) related to FP (black lines), IFP (blue lines), AS (red lines), and ASC (green lines) POs. The parts of adiabatic lines which are related to stable (unstable) POs are drawn by full (dashed) lines. The red dots mark the positions of anticrossings between the curves which are located along the adiabatic lines related to the AS PO.

Note that, since the IFP PO is always [i.e., for $E(R) < E_{\rm sp}(R)$] stable and since the AS and the ASC POs are stable in the ranges $E_{\rm sp}(R) < E(R) < E_{\rm bif}(R)$ and $E_{\rm bif}(R) < E(R) < 0.261/R$, respectively, the lower limiting line of each multiplet in the domain of negative energies is completely related to stable POs (see Fig. 12). We will see below that for this reason the nonadiabatic transitions between adiabatic states with different values of quantum number N (i.e., if $\Delta N \neq 0$) at negative energies are not related to these (IFP, AS, and ASC) classical configurations.

B. Anticrossings of adiabatic curves

The transitions of adiabatic curves of a given multiplet from the (IFP-AS,FP) area, where they are confined at large R, to the associated (ASC,AS) area are realized through a series of avoided crossings (anticrossings) between these curves. These anticrossings are located along the borderline between these two areas, i.e., along the part of the AS line where the AS orbit is unstable [31]. As can be seen from Fig. 11(a), on decreasing R the $(1,0)^+$ curve leaves the (IFP-AS,FP) area with $N = 2$, but the nearby $(-1,0)^+$ curve after that starts approaching the borderline (red). Essentially, due to the anticrossing between these two curves, it is the $(-1,0)^+$ curve which is at small R closer to the AS collinear configuration. The anticrossing positions (open red circles) are better visible in Fig. 13(a) where instead of adiabatic energies the corresponding adiabatic potentials are shown. A similar situation appears at the borderline (AS) for $N = 3$ where, due to anticrossings between the curves $(2,0)^+$, $(0,0)^+$, and $(-2,0)^+$, the first curve is closer to the AS configuration for large R and the third one at small R [see Figs. 12 and 13(a)]. This behavior is repeated in the vicinity of the AS adiabatic lines for each N, leading to $N-1$ successive anticrossings. However, the number of anticrossings along a given (Nth) AS line is in principle larger than $N-1$ because anticrossings between the adiabatic curves of different N also occur there.

A further inspection of Fig. 13(a) shows that another class of avoided crossings appears at positive adiabatic energies (i.e., at negative values of the adiabatic potential U). The positions of these antiscrossings (open green squares) indicate that they should be related to the ASC PO which becomes unstable for $E(R) > 0.261/R$ [i.e., for $U(R) < -0.522R$—the area below the green dotted line in Fig. 13(a)]. Note that some of these anticrossings coincide with the anticrossings of the previous (AS) class. In fact a number of anticrossings of adiabatic curves occur just at the positions where the adiabatic lines related to different types of POs cross mutually. One can see in Fig. 13(a) that such anticrossings occur at the positions where the ASC lines (their "unstable" parts) cross the AS as well as the FP lines. An ordered class of anticrossings related to the FP PO (FP type of hidden crossings), however, is not observed. This may be explained by the fact that the Lyapunov exponent for this PO after the value $\epsilon = -2.972$ rapidly grows with the scaled energy (see Fig. 6) and the classical dynamics in its neighborhood is highly chaotic (see Fig. 2). In this situation the corresponding branch points should lie deeply in the complex plane at very different distances from the real axis.

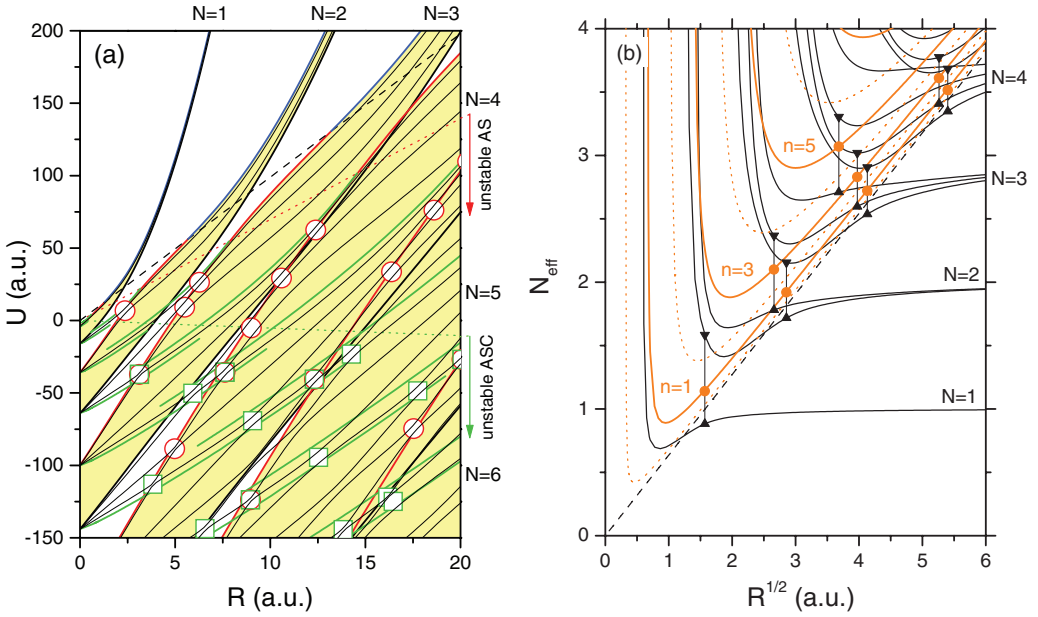

FIG. 13. (Color online) (a) The potential curves $U_\mu(R)$ related to symmetric adiabatic states of helium ($Z = 2$) with $L = 0$ (thin black lines) and the adiabatic potential lines $U_n(R)$ (for the same system) related to FP (black lines), IFP (blue lines), AS (red lines), and ASC (green lines) POs. The yellow areas are defined analogously as in Fig. 11(a). The black dashed line, the red dotted line, and the green dotted line correspond to the saddle point, to the AS-ASC bifurcation point, and to the stable-unstable separation point for the ASC PO, respectively. The open red circles mark the positions of anticrossings related to the AS PO [some of them are shown in Fig. 11(a)], whereas the open green squares mark those which are related to the ASC PO. (b) The adiabatic curves (thin black lines) and the adiabatic lines related to the Langmuir PO (orange lines) for the same system as in (a), shown as effective quantum numbers $N_{\text{eff}}(R)$. The orange dots mark the positions of anticrossings between the curves with $\Delta N = \Delta K = 1$, which are located along the adiabatic lines related to the Langmuir PO (here $n = N - K$).

A special class of anticrossings, which is best visible if we plot the adiabatic energies as effective quantum numbers, is that between the adiabatic curves belonging to nearby multiplets ($\Delta N = 1$) and located near the saddle-point line [see Fig. 13(b)]. Since in this area all of the considered fundamental POs are stable except the Langmuir one (see Fig. 6), without a deeper analysis one can predict that this class of anticrossings should be related to the motion on the Wannier ridge. This expectation is in agreement with the explanation for these anticrossings given in Ref. [14] (Sec. III.B.3.a.). The saddle-point energy, which is in Fig. 13(b) represented by the straight dashed line, in fact locates this class of anticrossings only approximately. The positions of these anticrossings are more precisely determined by the adiabatic lines related to the Langmuir PO, where the bending excitations above the saddle-point energy (labeled by the quantum number n) are taken into account. One can see in Fig. 13(b) that the L lines marked by odd values of the quantum number n are related to anticrossings between the curves with $\Delta N = \Delta K = 1$, whereby the anticrossings between the curves with $n = N - K$ are located along the nth line. Since the adiabatic curves belonging to nearby multiplets ($\Delta N = 1$) at the positions of their anticrossings are more separated than the curves from the same manifold ($\Delta N = 0$), which may also be related to the high instability of the Langmuir PO comparing to the AS and ASC POs, we can talk here about the L type of hidden crossings. This type of anticrossing can be related to the T type of hidden crossings which appears in the two-Coulomb-center problem (see, e.g., Ref. [8]), but which is also expected in the general case of Coulomb three-body systems [18].

V. SUMMARY AND CONCLUSIONS

In this paper we have analyzed properties of the hyperspherical adiabatic curves of helium for the total angular momentum equal to zero using classical dynamics as a tool. Since in the hyperspherical adiabatic approach the hyperradius R is an adiabatic variable, for each value of R the underlying classical dynamics reduces to the constrained two-electron motion lying on the hypersphere of this hyperradius. Then, for a given R, the 2D surface of the hypersphere is the corresponding configuration space $\{\alpha, \vartheta\}$. In a classical analysis, however, due to the scaling properties of Coulomb systems, it is more convenient to use the scaled energy $\epsilon = RE$ as the adiabatic parameter (instead of R).

The phase-space structure of the constrained two-electron motion at different values of ϵ is examined using the Poincaré surfaces-of-section technique. It is shown that five characteristic types of classical configurations exist, which are related to five types of short (fundamental) periodic orbits: the frozen planet PO, the inverted frozen planet PO, the asymmetric stretch PO, the asynchronous PO, and the Langmuir PO. All of these POs, except the IFP PO, have counterparts in the full (unconstrained) two-electron dynamics. The orbits belonging to the constrained and the unconstrained dynamics, however, can be very different in stability. In the case of motion on the hypersphere the stability of the POs depends on the scaled

energy, but in the full phase space of the helium atom the FP and Langmuir POs are always stable and the AS and ASC POs are always unstable. It is found that for $\epsilon < \epsilon_{sp}$, where $\epsilon_{sp} = -4.950$ is the saddle point of the scaled potential barrier (Wannier ridge), the classical dynamics on a hypersphere is nearly regular. At these scaled energies only the FP and IFP fundamental POs exist. In the range $\epsilon_{sp} < \epsilon < 0.261$ the FP, AS, and L POs change stability and the dynamics is mixed (regular, chaotic), whereas for positive energies (more precisely for $\epsilon > 0.261$) it practically becomes ergodic. An important value of the scaled energy is also $\epsilon_{bif} = -3.487$ when the stable AS PO (for $\epsilon < \epsilon_{bif}$) bifurcates to the unstable AS PO and the stable ASC PO. At higher scaled energies the ASC PO is the latest stable orbit which survives before the system becomes ergodic.

In order to study the correspondence between hyperspherical adiabatic curves and classical configurations on a hypersphere, the considered short POs (all five types) are quantized, giving as a result five families of so-called adiabatic lines (the energies of quantized POs as functions of R). The quantization is performed by taking into account only the degree of freedom along the corresponding trajectory, because these five types of POs are considered as fundamental modes of the two-electron motion on the hypersphere. The adiabatic lines obtained in this way are in many aspects similar to exact adiabatic curves, and a parallel analysis of these entities is useful for better understanding some features of the latter.

One of these features is the arrangement of adiabatic curves at large values of the hyperradius in multiplets characterized by the quantum number N. The Nth multiplet consists of the curves which for $R \to \infty$ converge to the Nth ionization threshold. The presented analysis has shown that each multiplet of $^1S^e$ (singlet, $L = 0$) adiabatic curves is, for sufficiently large R, delimited from the bottom and from the top by the adiabatic lines related to the IFP- AS and FP POs, respectively. These lines converge to the same ionization threshold as do the adiabatic curves of the corresponding multiplet. The parts of the IFP-AS line which are related to the IFP PO and to the stable AS PO are located below the saddle-point energy $E_{sp}(R) \equiv \epsilon_{sp}/R$ (large values of R) and in the area between $E_{sp}(R)$ and the bifurcation energy $E_{bif}(R) \equiv \epsilon_{bif}/R$ (medium range), respectively. The part of this line which is located above $E_{bif}(R)$ (small values of R) corresponds to the unstable AS PO. In this interval the adiabatic curves of a given multiplet cross the AS line and move to the area between the ASC and AS lines. Finally, since the ASC PO is stable at negative energies, it follows that the lower (IFP-AS-ASC) limiting line of each multiplet in the domain of negative energies is completely related to stable POs.

Recall here that the stable POs are always surrounded by stable phase-space areas (stability islands). Thus, some properties of the lower limiting line of the multiplet extrapolate to nearby adiabatic curves—they are in the domain of negative energies at *different* values of R related to *different* stable classical configurations. As a consequence, the quantum states of helium, which can be roughly determined by quantizing the R motion for each adiabatic curve [the quasiseparable approximation, which neglects the couplings between adiabatic curves (channels); see, e.g., Ref. [33]], in principle do *not* correspond to individual trajectories. From the semiclassical point of view, each quantum state contains contributions of classical configurations on hyperspheres with different values of the hyperradius R, taken from the interval of R between the turning points of R motion, which is determined by the corresponding adiabatic potential and the eigenenergy of this state. Such a correspondence between quantum states and classical trajectories is not new in the semiclassical approach. Gutzwiller has shown in his PO theory [34] that each quantum state of a chaotic system includes contributions of all POs of the system (for application to the helium atom, see Ref. [26]). However, the R mode, which is in the full dynamics of the helium atom the origin of instability (through the so-called triple collisions), in the adiabatic approach is stabilized (at least within the quasiseparable approximation), but, because R is not fixed, here different classical configurations contribute to each quantum state through intervals of different values of R.

Another feature of the adiabatic curves, which is analyzed in terms of classical configurations, is their avoided crossings (anticrossings). First, it is observed that the transitions of adiabatic curves of a given multiplet from the (IFP-AS,FP) area, where they are confined at large R, to the associated (ASC,AS) area (with a common AS line) are realized through a series of anticrossings between those curves which are located along the part of the AS line where the AS orbit is unstable. From the stability analysis it follows that the energy area where this type of anticrossing occurs is the area above the bifurcation energy $-3.487/R$, which is in agreement with the estimation $E(R) > -3.5/R$ given in Ref. [31]. Another class of anticrossings appears at positive adiabatic energies. They are related to the ASC PO which is unstable for $E(R) > 0.261/R$. These two classes of anticrossings may be compared to narrow avoided crossings, appearing mostly between curves of the same multiplet, which are typical for Coulomb three-body systems having comparable masses of charged particles [18]. In the case of helium, however, these anticrossings are not so narrow and they are organized in series. Thus, in these properties they are closer to hidden crossings. In addition, a number of avoided crossings of the adiabatic curves occurs at the positions where the adiabatic lines, which are related to different types of POs, cross mutually (e.g., ASC-AS and ASC-FP). An ordered class of anticrossings related to the FP PO (FP type of hidden crossings), however, is not observed, probably due to the rapid growth of its Lyapunov exponent with the scaled energy in the area where this orbit is unstable ($\epsilon > -2.972$).

A third class of anticrossings observed here, which can be related to an unstable PO, is that between the adiabatic curves belonging to nearby multiplets ($\Delta N = 1$). These anticrossings are located near the saddle point and can be related to the Langmuir PO (L type of hidden crossings). The fact that the adiabatic curves at the positions of these anticrossings are more separated (hidden crossings) than in the case of anticrossings of curves from the same manifold may be related to high instability of the Langmuir PO compared to the AS and ASC POs. On the other hand, the Lyapunov exponent for the Langmuir PO does not grow so rapidly with the scaled energy (in contrast to the FP PO) and the corresponding family of hidden crossings has a regular pattern.

The presented study clearly demonstrated the correspondence between several classes of avoided and hidden crossings

between the hyperspherical adiabatic curves of helium and unstable POs on a hypersphere, predicted in previous analyses of adiabatic curves of three-body Coulomb systems [18,19] and based on the semiclassical theory of hidden crossings [8]. In this paper most of the attention is given to the analysis of classical configurations on the hypersphere, allowing accurate determination of the corresponding adiabatic lines. The "unstable" parts of these lines can be identified as *diabatic* curves (potentials) [18], each of them connecting a series of avoided (hidden) crossings (characterized by the same quantum number n of the line) of a given class. The determination of diabatic curves can be especially helpful for finding and classifying hidden crossings of two-electron systems which are important for studying inelastic electron-atom collision processes.

ACKNOWLEDGMENTS

We want to thank Dr. O. I. Tolstikhin for providing us data containing numerically calculated adiabatic curves for the helium atom. This work is supported by Project No. 171020 of the Ministry of Education and Science of Serbia.

APPENDDIX: REGULARIZATION OF TWO-ELECTRON DYNAMICS ON A HYPERSPHERE

The Lagrangian which describes the constrained dynamics of a two-electron system on a hypersphere ($R = \text{const}$) in the case when $L = 0$ reads

$$\mathcal{L} = T - V = \frac{R^2}{2}\,(\dot{\alpha}^2 + \sin^2\alpha\cos^2\alpha\,\dot{\vartheta}^2) - \frac{C(\alpha,\vartheta)}{R}, \quad \text{(A1)}$$

where the function $C(\alpha,\vartheta)$ is given by Eq. (2). The associated Hamiltonian function has the form $H_R = T + V$, where the derivatives of coordinates α and ϑ in the kinetic energy term T must be replaced by the canonically conjugated momenta $P_\alpha = \partial\mathcal{L}/\partial\dot{\alpha} = R^2\dot{\alpha}$ and $P_\vartheta = \partial\mathcal{L}/\partial\dot{\vartheta} = R^2\sin^2\alpha\cos^2\alpha\,\dot{\vartheta}$; see Eq. (3) in Sec. II A. The potential V, however, has negative singularities at $\alpha = 0$ and $\pi/2$, and a direct numerical integration of the corresponding equations of motion fails for trajectories passing near these singularities. In addition, the potential has a positive singularity at $(\alpha,\vartheta) = (\pi/4,0)$, but here the infinite barrier (Coulomb repulsion) prevents the electrons from approaching each other sufficiently closely and the latter singularity in principle does not produce difficulties.

Since the Hamiltonian function (3) is invariant under the transformation $\alpha \to \pi/2 - \alpha$ ($\alpha = \pi/4$ is a symmetry axis; see Sec. II A), it is sufficient to calculate the trajectories in the fundamental domain $\alpha \in [0,\pi/4]$. In this case only the singularity at $\alpha = 0$ is one that should be regularized. In order to eliminate this singularity we introduce the variables

$$x = r\cos\vartheta, \quad y = r\sin\vartheta, \quad r = \tan\alpha \quad \text{(A2)}$$

and then express them in terms of semiparabolic coordinates u and v,

$$x = u^2 - v^2, \quad y = 2uv. \quad \text{(A3)}$$

From Eqs. (A2) and (A3) it follows that

$$r = (x^2 + y^2)^{1/2} = u^2 + v^2 \quad \text{(A4)}$$

and

$$\begin{aligned} \alpha &= \arctan(u^2 + v^2), \\ \vartheta &= \arctan\frac{2uv}{u^2 - v^2} \equiv 2\arctan\frac{v}{u}. \end{aligned} \quad \text{(A5)}$$

The inverse transformations are

$$u = \sqrt{\tan\alpha}\,\cos\vartheta/2, \quad v = \sqrt{\tan\alpha}\,\sin\vartheta/2. \quad \text{(A6)}$$

In the fundamental domain the variable r takes values from the interval $[0,1]$. Then $u^2 + v^2 \leqslant 1$ and, consequently, the fundamental domain in the (u,v) plane is the area limited by the unit circle.

Using relations (A5) we obtain expressions for the kinetic and potential energies [and thus for the Lagrangian (A1)] in semiparabolic coordinates,

$$T = \frac{2R^2 r}{(1+r^2)^2}\,(\dot{u}^2 + \dot{v}^2), \quad \text{(A7)}$$

$$V = -\frac{Z}{R}\sqrt{1+r^2}\left(1 + \frac{1}{r}\right) + \frac{1}{R\sqrt{1 - 2x/(1+r^2)}}, \quad \text{(A8)}$$

where x and r are the above-given functions of u and v. In the Hamiltonian function $H_R = T + V$, however, the kinetic energy term (A7) must be expressed in terms of the canonically conjugated momenta

$$P_u = \frac{\partial\mathcal{L}}{\partial\dot{u}} = \frac{\partial T}{\partial\dot{u}} = \frac{4R^2 r}{(1+r^2)^2}\,\dot{u}, \quad \text{(A9)}$$

$$P_v = \frac{\partial\mathcal{L}}{\partial\dot{v}} = \frac{\partial T}{\partial\dot{v}} = \frac{4R^2 r}{(1+r^2)^2}\,\dot{v}. \quad \text{(A10)}$$

Using these expressions one obtains

$$T = \frac{(1+r^2)^2}{8R^2 r}\left(P_u^2 + P_v^2\right). \quad \text{(A11)}$$

Note, however, that singularities are not removed simply by introducing new variables. In order to eliminate the singularity at $\alpha = 0$ ($r = 0$) we introduce the new time variable $\tilde{t}$, defined as

$$dt = r\,d\tilde{t}, \quad \text{(A12)}$$

and the new (regularized) Hamiltonian function

$$\tilde{H} = r(H_R - E) \equiv 0. \quad \text{(A13)}$$

The latter quantity is a constant of motion (with the so-called pseudoenergy equal to zero), which ensures that the corresponding equations of motion preserve the canonical form. It can be written as the sum $\tilde{H} = \tilde{T} + \tilde{V}$, where

$$\tilde{T} = rT = \frac{2R^2}{(1+r^2)^2}\left[\left(\frac{du}{d\tilde{t}}\right)^2 + \left(\frac{dv}{d\tilde{t}}\right)^2\right], \quad \text{(A14)}$$

$$\begin{aligned} \tilde{V} &= r(V - E) \\ &= -\frac{Z}{R}\sqrt{1+r^2}\,(1+r) + \frac{r}{R\sqrt{1 - 2x/(1+r^2)}} - rE. \end{aligned} \quad \text{(A15)}$$

The kinetic energy term $\tilde{T}$ in the new Hamiltonian function, however, must be given in the canonical form. For this reason we construct the Lagrangian $\tilde{\mathcal{L}} = \tilde{T} - \tilde{V}$ and introduce the appropriate canonical momenta as $\tilde{P}_u = \partial\tilde{\mathcal{L}}/\partial(du/d\tilde{t})$ and $\tilde{P}_v = \partial\tilde{\mathcal{L}}/\partial(dv/d\tilde{t})$. It follows, however, that these coincide with the former momenta,

$$\tilde{P}_u = \frac{4R^2}{(1+r^2)^2}\frac{du}{d\tilde{t}} = \frac{4R^2 r}{(1+r^2)^2}\frac{du}{dt} = P_u, \tag{A16}$$

$$\tilde{P}_v = \frac{4R^2}{(1+r^2)^2}\frac{dv}{d\tilde{t}} = \frac{4R^2 r}{(1+r^2)^2}\frac{dv}{dt} = P_v. \tag{A17}$$

Using these relations the kinetic energy $\tilde{T}$ is transformed to the form

$$\tilde{T} = \frac{(1+r^2)^2}{8R^2}\left(P_u^2 + P_v^2\right). \tag{A18}$$

Finally, the new Hamiltonian function is

$$\tilde{H}(P_u, P_v, u, v) = \tilde{T} + \tilde{V}, \tag{A19}$$

where $\tilde{T}$ and $\tilde{V}$ are given by Eqs. (A18) and (A15), respectively.

The Hamilton equations obtained using the Hamiltonian function (A19) and the new time variable $\tilde{t}$ read

$$\frac{du}{d\tilde{t}} = \frac{\partial\tilde{H}}{\partial P_u} \equiv \frac{(1+r^2)^2}{4R^2}P_u, \tag{A20}$$

$$\frac{dv}{d\tilde{t}} = \frac{\partial\tilde{H}}{\partial P_v} \equiv \frac{(1+r^2)^2}{4R^2}P_v, \tag{A21}$$

$$\frac{dP_u}{d\tilde{t}} = -\frac{\partial\tilde{H}}{\partial u} \equiv -\frac{r(1+r^2)u}{R^2}\left(P_u^2 + P_v^2\right) - \frac{\partial\tilde{V}}{\partial u}, \tag{A22}$$

$$\frac{dP_v}{d\tilde{t}} = -\frac{\partial\tilde{H}}{\partial v} \equiv -\frac{r(1+r^2)v}{R^2}\left(P_u^2 + P_v^2\right) - \frac{\partial\tilde{V}}{\partial v}. \tag{A23}$$

In order to get the trajectories that are solutions of these equations of motion, but in real time t, Eq. (A12) must be integrated simultaneously with Eqs. (A20)–(A23). Then the trajectories in hyperspherical coordinates can be obtained using transformations (A5) and

$$P_\alpha = \frac{1+r^2}{2r}(uP_u + vP_v), \tag{A24}$$

$$P_\vartheta = \frac{1}{2}(uP_v - vP_u). \tag{A25}$$

The inverse transformations are

$$P_u = 2\left(\frac{uP_\alpha}{1+r^2} - \frac{vP_\theta}{r}\right), \tag{A26}$$

$$P_v = 2\left(\frac{vP_\alpha}{1+r^2} + \frac{uP_\theta}{r}\right). \tag{A27}$$

If a trajectory which starts inside the fundamental domain is approaching the borderline (symmetry axis) $\alpha = \pi/4$ (i.e., if $r \to 1$) with a nonvanishing momentum P_α, in order to keep the trajectory inside the domain we have to change the sign of P_α at $\alpha = \pi/4$ (reflection at the symmetry axis). Otherwise, the trajectory would leave the fundamental domain and eventually approach the singularity at $\alpha = \pi/2$. The trajectory in the full domain ($0 \leqslant \alpha \leqslant \pi/2$), however, can be obtained easily from the trajectory in the fundamental domain by applying the transformations $\alpha \to \pi/2 - \alpha$, $P_\alpha \to -P_\alpha$ to all segments of the latter which are between an odd and the succeeding (even) reflection.

If we want to show the two-electron trajectories in Cartesian coordinates after integrating Eqs. (A20)–(A23), we need to determine the azimuthal angles ϑ_1 and ϑ_2 for individual electrons (then $x_i = r_i\cos\vartheta_i$, $y_i = r_i\sin\vartheta_i$, where $r_1 = R\cos\alpha$, $r_2 = R\sin\alpha$) instead of the mutual angle $\vartheta = \vartheta_1 - \vartheta_2$. From the condition $\cos^2\alpha\,\dot{\vartheta}_1 + \sin^2\alpha\,\dot{\vartheta}_2 = 0$, which holds for $L = 0$ ($L = r_1^2\dot{\vartheta}_1 + r_2^2\dot{\vartheta}_2$), and the relation $\dot{\vartheta} = \dot{\vartheta}_1 - \dot{\vartheta}_2$ one obtains $\dot{\vartheta}_1 = \sin^2\alpha\,\dot{\vartheta}$ and $\dot{\vartheta}_2 = -\cos^2\alpha\,\dot{\vartheta}$. In order to solve these equations, their right-hand sides should be expressed in terms of semiparabolic coordinates. From the expression for ϑ given in Eq. (A5) and relations (A9) and (A10) we have

$$\dot{\vartheta} = \frac{2}{r}(u\dot{v} - v\dot{u}) = \frac{(1+r^2)^2}{2R^2r^2}(uP_v - vP_u). \tag{A28}$$

Finally, using the new time variable the equations for ϑ_1 and ϑ_2 become

$$\frac{d\vartheta_1}{d\tilde{t}} = \frac{r(1+r^2)}{2R^2}(uP_v - vP_u), \tag{A29}$$

$$\frac{d\vartheta_2}{d\tilde{t}} = -\frac{1+r^2}{2R^2r}(uP_v - vP_u). \tag{A30}$$

Then the angles ϑ_1 and ϑ_2 can be obtained by integrating one of these equations simultaneously with Eqs. (A20)–(A23).

[1] M. Born and V. Fock, Z. Phys. **51**, 165 (1928).
[2] J. von Neumann and E. P. Wigner, Physik. Z. **30**, 467 (1929).
[3] E. A. Solov'ev, Sov. Phys. Usp. **32**, 228 (1989).
[4] L. D. Landau, Phys. Z. Sowjetunion **1**, 88 (1932).
[5] C. Zener, Proc. R. Soc. London, Ser. A **137**, 696 (1932).
[6] E. A. Solov'ev, Sov. Phys. JETP **54**, 893 (1981).
[7] E. A. Solov'ev, Sov. Phys. JETP **63**, 678 (1986).
[8] E. A. Solov'ev, J. Phys. B **38**, R153 (2005).
[9] J. Macek, J. Phys. B **2**, 831 (1968).
[10] D. R. Herrick, Adv. Chem. Phys. **52**, 1 (1983).
[11] C. D. Lin, Phys. Rev. Lett. **51**, 1348 (1983); Phys. Rev. A **29**, 1019 (1984).
[12] C. D. Lin, Phys. Rep. **257**, 1 (1995).
[13] J-M. Rost and J. S. Briggs, J. Phys. B **24**, 4293 (1991).
[14] G. Tanner, K. Richter, and J-M. Rost, Rev. Mod. Phys. **72**, 497 (2000).
[15] J. H. Macek, S. Yu. Ovchinnikov, and S. V. Pasovets, Phys. Rev. Lett. **74**, 4631 (1995).
[16] J. H. Macek and S. Yu. Ovchinnikov, Phys. Rev. A **54**, 544 (1996).
[17] S. J. Ward, J. H. Macek, and S. Yu. Ovchinnikov, Phys. Rev. A **59**, 4418 (1999).
[18] E. A. Solov'ev and O. I. Tolstikhin, J. Phys. B **34**, L439 (2001).
[19] E. A. Solov'ev, Eur. Phys. J. D **65**, 331 (2011).

[20] K. Richter, G. Tanner, and D. Wintgen, Phys. Rev. A **48**, 4182 (1993).
[21] H. D. Meyer, J. Chem. Phys. **84**, 3147 (1986).
[22] S. Watanabe, Phys. Rev. A **36**, 1566 (1987).
[23] K. Richter and D. Wintgen, Phys. Rev. Lett. **65**, 1965 (1990).
[24] P. Grujić and N. Simonović, J. Phys. B **24**, 5055 (1991).
[25] J. Langmuir, Phys. Rev. **17**, 339 (1921).
[26] D. Wintgen, K. Richter, and G. Tanner, Chaos **2**, 19 (1992).
[27] N. S. Simonović, Chaos **9**, 854 (1999); Few-Body Systems **32**, 183 (2003).
[28] E. A. Solov'ev, Sov. Phys. JETP **62**, 1148 (1985); in *Classical Dynamics in Atomic and Molecular Physics*, edited by T. Grozdanov, P. Grujić, and P. Krstić (World Scientific, Singapore, 1989), pp. 84–104.
[29] P. Grujić and N. Simonović, J. Phys. B **28**, 1159 (1995).
[30] M. P. Strand and W. P. Reinhardt, J. Chem. Phys. **70**, 3812 (1979).
[31] N. S. Simonović, J. Phys. B **44**, 105004 (2011).
[32] H. Friedrich, *Theoretical Atomic Physics* (Springer, Berlin, 2006).
[33] A. F. Starace, in *Fundamental Processes in Atomic Dynamics*, edited by J. S. Briggs, H. Kleinpoppen, and H. O. Lutz (Plenum, New York, 1988), p. 235.
[34] M. C. Gutzwiller, *Chaos in Classical and Quantum Mechanics* (Springer, New York, 1990).